NAVAL POSTGRADUATE SCHOOL

MONTEREY, CALIFORNIA

THESIS

FLEXIBLE MULTI-BODY SPACECRAFT SIMULATOR: DESIGN, CONSTRUCTION, AND EXPERIMENTS

by

Adam L. Atwood

December 2017

Thesis Advisor: Mark Karpenko
Second Reader: I. Michael Ross

THIS PAGE INTENTIONALLY LEFT BLANK

REPORT DOCUMENTATION PAGE			*Form Approved OMB No. 0704-0188*

1. AGENCY USE ONLY *(Leave blank)*	**2. REPORT DATE** December 2017	**3. REPORT TYPE AND DATES COVERED** Master's thesis

4. TITLE AND SUBTITLE
FLEXIBLE MULTI-BODY SPACECRAFT SIMULATOR: DESIGN, CONSTRUCTION, AND EXPERIMENTS

5. FUNDING NUMBERS

6. AUTHOR(S) Adam L. Atwood

7. PERFORMING ORGANIZATION NAME(S) AND ADDRESS(ES)
Naval Postgraduate School
Monterey, CA 93943-5000

8. PERFORMING ORGANIZATION REPORT NUMBER

9. SPONSORING /MONITORING AGENCY NAME(S) AND ADDRESS(ES)
N/A

10. SPONSORING / MONITORING AGENCY REPORT NUMBER

11. SUPPLEMENTARY NOTES The views expressed in this thesis are those of the author and do not reflect the official policy or position of the Department of Defense or the U.S. Government. IRB number ____N/A____.

12a. DISTRIBUTION / AVAILABILITY STATEMENT
Approved for public release. Distribution is unlimited.

12b. DISTRIBUTION CODE

13. ABSTRACT (maximum 200 words)

The aim of this thesis was to develop and construct a flexible multi-body spacecraft simulator for use in testing optimal control-based slew and maneuver designs. The simulator is modified from an earlier prototype, which had a flexible arm and actuated robotic arm on an aluminum plate atop an air bearing. The new simulator features enhanced capabilities, with an improved passive flexible appendage, a commercial-off-the-shelf (COTS) robotic arm, a reaction wheel momentum control system, a wireless flight control system, and a battery-powered electrical distribution system. The COTS robotic arm was modified to function with either flexible or rigid joints, and was used as a basis for initial experimentation. The simulator's purpose is to test agile cooperative maneuvers designed using optimal control theory. A specific maneuver was developed and tested for the robotic arm in its flexible joint configuration. It is shown experimentally that maneuver time could be reduced by 50% as compared to a baseline (standard) maneuver, and that the optimal control-based solution significantly reduced post-maneuver vibrations.

14. SUBJECT TERMS optimal control, flexible space system, multi-body, satellite, vibrations	**15. NUMBER OF PAGES** 99
	16. PRICE CODE

17. SECURITY CLASSIFICATION OF REPORT	**18. SECURITY CLASSIFICATION OF THIS PAGE**	**19. SECURITY CLASSIFICATION OF ABSTRACT**	**20. LIMITATION OF ABSTRACT**
Unclassified	Unclassified	Unclassified	UU

NSN 7540-01-280-5500 Standard Form 298 (Rev. 2-89)
Prescribed by ANSI Std. 239-18

THIS PAGE INTENTIONALLY LEFT BLANK

Approved for public release. Distribution is unlimited.

FLEXIBLE MULTI-BODY SPACECRAFT SIMULATOR: DESIGN, CONSTRUCTION, AND EXPERIMENTS

Adam L. Atwood
Lieutenant, United States Navy
B.S., United States Naval Academy, 2010

Submitted in partial fulfillment of the
requirements for the degree of

MASTER OF SCIENCE IN ASTRONAUTICAL ENGINEERING

from the

NAVAL POSTGRADUATE SCHOOL
December 2017

Approved by: Mark Karpenko
Thesis Advisor

I. Michael Ross
Second Reader

Garth V. Hobson
Chair, Department of Mechanical and Aerospace Engineering

THIS PAGE INTENTIONALLY LEFT BLANK

ABSTRACT

The aim of this thesis was to develop and construct a flexible multi-body spacecraft simulator for use in testing optimal control-based slew and maneuver designs. The simulator is modified from an earlier prototype, which had a flexible arm and actuated robotic arm on an aluminum plate atop an air bearing. The new simulator features enhanced capabilities, with an improved passive flexible appendage, a commercial-off-the-shelf (COTS) robotic arm, a reaction wheel momentum control system, a wireless flight control system, and a battery-powered electrical distribution system. The COTS robotic arm was modified to function with either flexible or rigid joints, and was used as a basis for initial experimentation. The simulator's purpose is to test agile cooperative maneuvers designed using optimal control theory. A specific maneuver was developed and tested for the robotic arm in its flexible joint configuration. It is shown experimentally that maneuver time could be reduced by 50% as compared to a baseline (standard) maneuver, and that the optimal control-based solution significantly reduced post-maneuver vibrations.

THIS PAGE INTENTIONALLY LEFT BLANK

TABLE OF CONTENTS

LIST OF FIGURES

LIST OF TABLES

THIS PAGE INTENTIONALLY LEFT BLANK

LIST OF ACRONYMS AND ABBREVIATIONS

2DOFSFJ	2DOF serial flexible joint
3D	3-dimensional
cRIO	compact reconfigurable input/output real-time controller
DC	direct current
DOF	degree of freedom
FPGA	field-programmable gate array
KKT	Karush-Kuhn-Tucker
LQR	linear quadratic regulator
MBSS	multi-body flexible spacecraft simulator
MCS	momentum control system
NI	national instruments
NPS	Naval Postgraduate School
PD	proportional derivative controller
QUARC	Quanser real-time control
RPC	Rapid Prototyping Center

THIS PAGE INTENTIONALLY LEFT BLANK

ACKNOWLEDGMENTS

I would like to thank my advisors, Professor Karpenko and Distinguished Professor Ross, for their support, guidance, and patience during this thesis process. I would also like to thank Mr. John Mobley with the NPS machine shop and Mr. Dan Sakoda with the Rapid Prototyping Center for their assistance in manufacturing the actual structure of the testbed.

THIS PAGE INTENTIONALLY LEFT BLANK

I. INTRODUCTION

A. MOTIVATION

As demand on spacecraft increase, moveable appendages such as robotic manipulators and articulated antennae will play an increasingly important role for future satellite missions. As a whole, the satellite bus and its appendages can be considered as a multi-body system [1]. Motion control of such dynamical systems is a challenging task. Part of the difficulty arises from the various coupled interactions that occur between the bodies. For example, the motion of one link in a multi-body system induces motion in the others. Rapidly moving some of the bodies, such as quickly slewing an antenna to a new orientation, exacerbates the coupling effects between the links. Consequently, it can be difficult to maintain precise control over the nominally stationary links if it is required to move the others quickly unless the disturbances can be properly attenuated [2]–[4]. Flexible effects make matters worse because higher-bandwidth control is needed to suppress the troublesome flexible modes. Such high gain controls are often undesirable as noise and other unwanted effects can be amplified. To manage the flexible motion control problem using lower gain control, a common approach is to limit the accelerations and rates of the links in order to bound the disturbance magnitude to an acceptable level [5]. Doing so makes it easier to design lower-bandwidth control systems that can properly reject the effects of the undesirable dynamics. However, this convenience comes at the expense of decreased system agility and sluggish response.

An alternative approach is to apply optimal control theory to the multi-body system as a whole in order to design cooperative motion trajectories that account for the internal coupling of the system dynamics [5]–[9]. This approach allows the various dynamic interactions to be accommodated from a different point of view: instead of treating dynamic coupling effects as disturbances to be rejected amongst the various subsystems, optimal control can make use of dynamic coupling effects advantageously to compensate for the induced disturbances. The previous work [5]–[9], however, considers only rigid body motion of multi-body systems.

The goal of this thesis is to further develop the optimal control concept presented in [5] to handle systems with flexible effects so that proper control over the flexible motion can be realized even when moving links quickly. To this end, a test bed is developed which allows for flexible motion control experiments to be carried out in a laboratory environment. The multi-body system test bed comprises a two-link rigid/flexible manipulator, a two-link rigid manipulator, a passive flexible link and a reaction wheel momentum control system all mounted to a single degree-of-freedom air bearing, as well as all of the support electronics. This system can be modeled and controlled as a multi-body, flexible, dynamical system.

B. OBJECTIVE AND SCOPE

This thesis will examine the feasibility of performing rapid maneuvers of a flexible multi-body system. To achieve this, the thesis will follow the pathway of first constructing a mathematical model of an idealized system. Second, a spacecraft simulator testbed (initially constructed as part of a prior thesis [10]) will be modified and improved to allow for the necessary experimentation. The nominal mathematical model for the initial proof of concept experiment will then be modified to more accurately reflect the behavior of the physical system. Finally, the optimal control maneuver will be tested and analyzed experimentally.

The ultimate goal of the greater research endeavor, of which this thesis is but one link in the chain, is to test optimal control maneuvers on real satellites involving actuated devices such as steerable antennae, other flexible antennae, and the satellite's own momentum control system. This thesis, however, will be limited to determining the feasibility of a single optimal control maneuver of a robotic arm on a fixed base. This is because the optimal control concept has not been experimentally tested, even for a two-link system. The results will serve as the basis for future experiments involving the entire system. To this end, required upgrades to an existing testbed will be made to allow this future work to be carried out.

C. THESIS OUTLINE

To facilitate a clear understanding of the thesis goals and results, the thesis will be arranged to reflect the research progression. The motivation for performing this research is to make satellites more capable and responsive via advanced motion control concepts in order to enhance their overall utility and mission throughput. This motivation leads to the requirement to determine whether such a concept is theoretically possible, discussed in Chapter II. Upon determination that such a course of action is feasible, the testbed is developed to test the ideas in practice. The various components and design is discussed in Chapter III. Chapter IV is given to the robotic arm that is used, as this is an integral part of the experiment. The already-discussed optimal control maneuver is then adapted to the physical system and demonstrated in the lab setting, the results of which are discussed in Chapter V. Finally, Chapter VI discussed future work. This is important to illustrate the steps that have been taken so far, the current state of the project, and the road ahead to the ultimate conclusion of the goal of rapidly maneuvering satellites.

THIS PAGE INTENTIONALLY LEFT BLANK

II. RAPID MOTION CONTROL OF FLEXIBLE MULTI-BODY SYSTEM: PROOF OF CONCEPT

Before the broader thesis objectives of testing flexible multi-body systems can take place, it is important to verify theoretically that such a concept is even feasible. In order to enable the thesis research objectives, a mathematical model of the multi-body dynamical system needs to be created. This model will then be used to test the optimal control principles. This chapter will build the mathematical model of the system, and then do initial feasibility verification and validation to ensure that the rest of the thesis has a solid foundation on which to build.

A. GENERAL EQUATIONS FOR MULTI-BODY DYNAMICS

A generic three-body dynamic system with two gimbaled joints is shown in Figure 1.

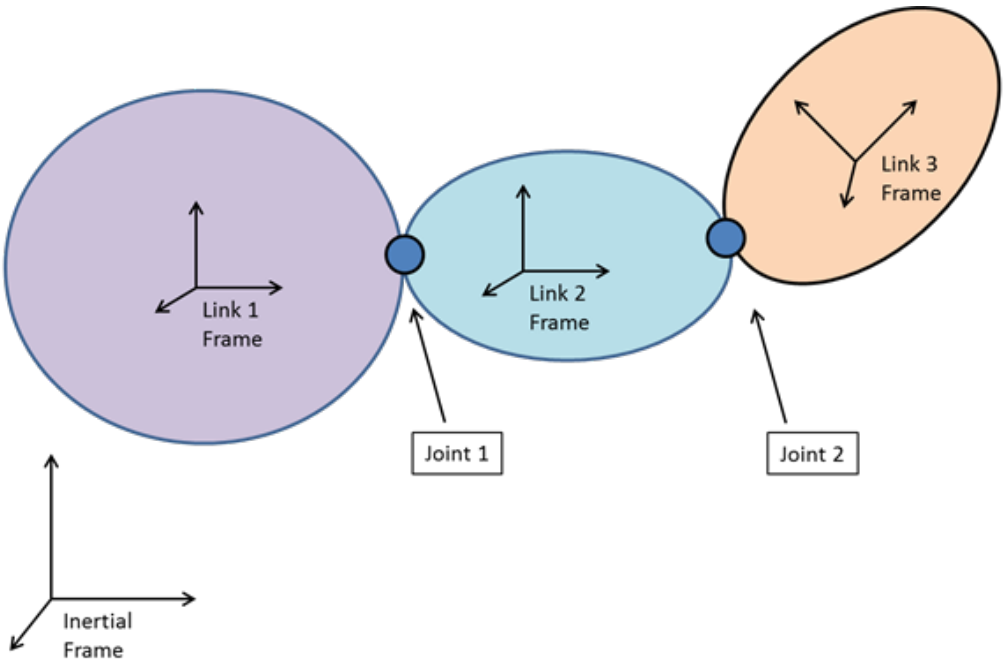

Figure 1. A multi-body dynamic system with two gimbaled joints

Considering each body separately, the Newton-Euler equations may be written as [1]

$$\begin{aligned} m_1\dot{v}_1 &= F_1 - F_{G1} \\ m_2\dot{v}_2 &= F_2 + F_{G1} - F_{G2} \\ m_3\dot{v}_3 &= F_3 + F_{G2} \end{aligned} \tag{1.1}$$

$$\begin{aligned} I_1\dot{\omega}_1 &= T_1 - T_{G1} - (r_{11}\times F_{G1}) - (\omega_1 \times I_1\omega_1) \\ I_2\dot{\omega}_2 &= T_2 + T_{G1} - T_{G2} + (r_{21}\times F_{G1}) - (r_{22}\times F_{G2}) - (\omega_2 \times I_2\omega_2), \\ I_3\dot{\omega}_3 &= T_3 + T_{G2} + (r_{32}\times F_{G2}) - (\omega_3 \times I_3\omega_3) \end{aligned} \tag{1.2}$$

where the meanings of the symbols for each body are listed in Table 1.

Casting the variables in appropriate frames and manipulating the equations to eliminate the joint constraint forces, allows the equations of motion to be written in the following state-space form:

$$\dot{x} = \begin{bmatrix} \dot{\omega} \\ \dot{\alpha}_r \\ \dot{\beta}_r \end{bmatrix} = (A - RU^{-1}S)^{-1}(T - RU^{-1}F), \tag{1.3}$$

where ω is the angular rate of the base link (body 1), α_r is the angle rate of the first gimbal and β_r is the angle rate of the second gimbal.

Table 1. Symbols used in Newton-Euler equations

Symbol	Description
$\omega_1, \omega_2, \omega_3$	Angular velocity
v_1, v_2, v_3	Velocity of the mass center
I_1, I_2, I_3	Central moments of inertia
m_1, m_2, m_3	Mass
$r_{11}, r_{21}, r_{22}, r_{32}$	Vector from mass center *i* to joint *j*
F_1, F_2, F_3	Resultant external force
T_1, T_2, T_3	Resultant external torque
F_{G1}, F_{G2}	Joint constraint force
T_{G1}, T_{G2}	Joint torque

B. DYNAMIC MODEL OF FLEXIBLE MANIPULATOR SUBSYSTEM

The general model of a multi-body system given in (1.3) can be applied to a flexible manipulator. Previous thesis research has produced a two-link robotic arm, constructed of aluminum and powered by DC motors at each joint [10]. In this chapter a mathematical model will be derived using an idealized version of this system. Pending successful results of the analysis, a version of this mathematical model will be used for experimentation on the multi-body flexible spacecraft simulator (MBSS) testbed. A basic illustration of the system is shown in Figure 2.

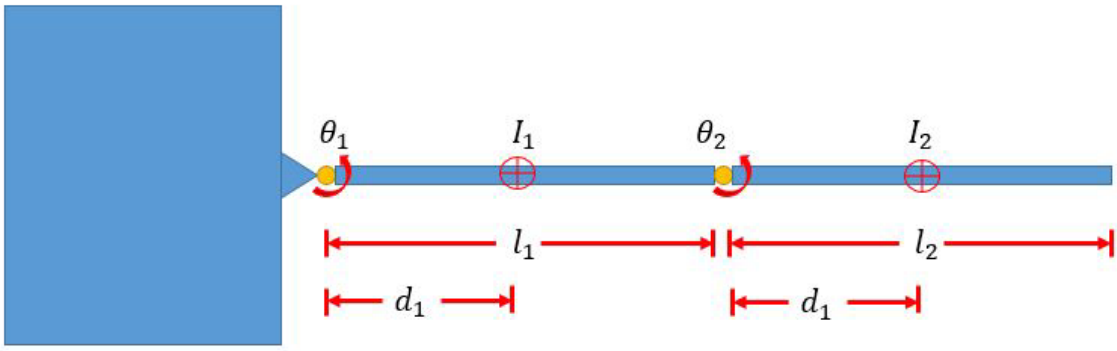

Figure 2. Basic schematic of two-link manipulator with fixed base

The dynamical equations that describe the motion can be derived through application of (1.1) to (1.3), the multi-body dynamics described in the previous section. The results are shown in the rigid body equations below, as adapted from [11].

$$\begin{aligned} m_{11}\ddot{\theta}_1 + m_{12}\ddot{\theta}_2 - 2r\dot{\theta}_1\dot{\theta}_2 - r\dot{\theta}_2^2 = 0 \\ m_{21}\ddot{\theta}_1 + m_{22}\ddot{\theta}_2 + r\dot{\theta}_1^2 = 0 \end{aligned} \tag{1.4}$$

As shown in [11], the system dynamics can be written in matrix form, to also include the flexibility associated with the rotors. The **M**, **C**, and **K** in equation (1.5) are matrices. **M** is the mass matrix, which accounts for mass and moment of inertia, **C** combines the Coriolis matrix with the damping force, and **K** contains the spring constants.

$$\begin{aligned} \mathbf{M}_1\ddot{\theta} + \mathbf{C}(\dot{\theta} - \dot{\varphi}) + \mathbf{K}(\theta - \varphi) &= 0 \\ \mathbf{M}_2\ddot{\theta} - \mathbf{C}(\dot{\theta} - \dot{\varphi}) - \mathbf{K}(\theta - \varphi) &= \tau \end{aligned} \tag{1.5}$$

The dynamical equations (1.4) are substituted into the matrix equations (1.5), giving a nonlinear equation of the form of equation (1.6).

$$\begin{bmatrix} m_{11} & m_{12} & 0 & 0 \\ m_{21} & m_{22} & 0 & 0 \\ 0 & 0 & I_r & 0 \\ 0 & 0 & 0 & I_r \end{bmatrix} \begin{bmatrix} \ddot{\theta}_1 \\ \ddot{\theta}_2 \\ \ddot{\varphi}_1 \\ \ddot{\varphi}_2 \end{bmatrix} + \begin{bmatrix} -2r\dot{\theta}_2 + c & -r\dot{\theta}_2 & -c & 0 \\ r\dot{\theta}_1 & c & 0 & -c \\ -c & 0 & c & 0 \\ 0 & -c & 0 & c \end{bmatrix} \begin{bmatrix} \dot{\theta}_1 \\ \dot{\theta}_2 \\ \dot{\varphi}_1 \\ \dot{\varphi}_2 \end{bmatrix} + \begin{bmatrix} k & 0 & -k & 0 \\ 0 & k & 0 & -k \\ -k & 0 & k & 0 \\ 0 & -k & 0 & k \end{bmatrix} \begin{bmatrix} \theta_1 \\ \theta_2 \\ \varphi_1 \\ \varphi_2 \end{bmatrix} = \begin{bmatrix} 0 \\ 0 \\ \tau_1 \\ \tau_2 \end{bmatrix} \tag{1.6}$$

In the equations above, the elements of the mass matrix and the Coriolis/centripetal parameters are shown in equations (1.7)–(1.10):

$$m_{11} = I_1 + I_2 + m_1 l_1^2 + m_2(d_1^2 + l_2^2 + 2d_1 d_2 cos\theta_2) \tag{1.7}$$

$$m_{12} = m_{21} = I_2 + m_2(l_2^2 + d_1 l_2 cos\theta_2) \tag{1.8}$$

$$m_{22} = I_2 + m_2 l_2^2 \tag{1.9}$$

$$r = m_2 l_1 l_2 \sin\theta_2, \tag{1.10}$$

where I is the mass moment of inertia of the link, m_i is the mass of link i, l is the length, and d is the distance from the end to the center of mass (see Figure 2). An idealized system is used for this analysis, and the values of these parameters are shown in Table 2.

Table 2. Idealized physical parameters of two-link flexible arm

Symbol	Description	Value
I_1, I_2	Link moment of inertia	10 kg·m^2
I_r	Rotor moment of inertia	1 kg·m^2
l_1, l_2	Link length	1 m
d_1, d_2	Link distance from axis of rotation to center of mass	0.5 m
m_1, m_2	Link mass	1 kg
c	Damping coefficient	1 Nms/rad
k	Spring constant	1 N/m

Equation (1.6) could be used directly to construct an optimal control problem for maneuver planning, but the nonlinearities make this difficult, hence they are normally not considered. That is, in standard practice the equations are decoupled. To accommodate the nonlinearities, equation (1.4) is rewritten with the nonlinear elements collected on the right-hand side. Retaining the nonlinear terms ensures that the effects of these elements can be considered as part of the maneuver design. The right hand side can then be relabeled as a virtual torque inputs $\tilde{\tau}$, as shown in equations (1.11) and (1.12). This approach is modified from [10] and [12].

$$\tilde{\tau}_1 = -2m_2 d_1 d_2 cos(\theta_2)\ddot{\theta}_1 - m_2 d_1 l_2 cos(\theta_2)\ddot{\theta}_2 - 2m_2 l_1 l_2 sin(\theta_2)\dot{\theta}_2\dot{\theta}_1 + m_2 l_1 l_2 sin(\theta_2)\dot{\theta}_2^2 \quad (1.11)$$

$$\tilde{\tau}_2 = -m_2 d_1 l_2 cos(\theta_2)\ddot{\theta}_1 - m_2 l_1 l_2 sin(\theta_2)\dot{\theta}_1^2 \quad (1.12)$$

These new torques are used to rewrite the dynamics equation as:

$$[\mathbf{M}]\begin{bmatrix}\ddot{\theta}_1\\ \ddot{\theta}_2\\ \ddot{\varphi}_1\\ \ddot{\varphi}_2\end{bmatrix}+[\mathbf{C}]\begin{bmatrix}\dot{\theta}_1\\ \dot{\theta}_2\\ \dot{\varphi}_1\\ \dot{\varphi}_2\end{bmatrix}+[\mathbf{K}]\begin{bmatrix}\theta_1\\ \theta_2\\ \varphi_1\\ \varphi_2\end{bmatrix}=\begin{bmatrix}\tilde{\tau}_1\\ \tilde{\tau}_2\\ \tau_1\\ \tau_2\end{bmatrix}, \tag{1.13}$$

where [**M**], [**C**], and [**K**] are now all linear matrices with constant parameters. The precise values of $\tilde{\tau}_i$ can be determined by enforcing a set of differential algebraic constants. This will be discussed in detail later.

Equation (1.13) can now be manipulated to isolate the second derivatives as shown in (1.14).

$$\begin{bmatrix}\ddot{\theta}_1\\ \ddot{\theta}_2\\ \ddot{\varphi}_1\\ \ddot{\varphi}_2\end{bmatrix}=[\mathbf{M}]^{-1}\left\{\begin{bmatrix}\tilde{\tau}_1\\ \tilde{\tau}_2\\ \tau_1\\ \tau_2\end{bmatrix}-[\mathbf{C}]\begin{bmatrix}\dot{\theta}_1\\ \dot{\theta}_2\\ \dot{\varphi}_1\\ \dot{\varphi}_2\end{bmatrix}-[\mathbf{K}]\begin{bmatrix}\theta_1\\ \theta_2\\ \varphi_1\\ \varphi_2\end{bmatrix}\right\} \tag{1.14}$$

The second derivatives are expounded in equation (1.15).

$$\begin{bmatrix}\ddot{\theta}_1\\ \ddot{\theta}_2\\ \ddot{\varphi}_1\\ \ddot{\varphi}_2\end{bmatrix}=\begin{bmatrix}\dfrac{4(\varphi_1-\varphi_2+\dot{\varphi}_1-\dot{\varphi}_2+\tilde{\tau}_1-\tilde{\tau}_2-\theta_1+\theta_2-\dot{\theta}_1-\dot{\theta}_2)}{45}\\ \dfrac{4(-\varphi_1-\dot{\varphi}_1-\dot{\varphi}_2-\tilde{\tau}_1+\dot{\theta}_1+\dot{\theta}_2)}{45}+\dfrac{89(\varphi_2+\dot{\varphi}_2+\tilde{\tau}_2-\theta_2-\dot{\theta}_2}{495}\\ \tau_1-\dot{\varphi}_1-\varphi_1+\theta_1+\dot{\theta}_1\\ \tau_2-\dot{\varphi}_2-\varphi_2+\theta_2+\dot{\theta}_2\end{bmatrix} \tag{1.15}$$

Now that the second derivatives have been found, the state space model of the entire system can be written, as in equation (1.16). This model will be used to formulate the optimal control problem for rapid maneuvering.

$$\dot{x} = f(x,u,t) = \begin{bmatrix} \dot{\theta}_1 \\ \dot{\theta}_2 \\ \dot{\varphi}_1 \\ \dot{\varphi}_2 \\ \ddot{\theta}_1 \\ \ddot{\theta}_2 \\ \ddot{\varphi}_1 \\ \ddot{\varphi}_2 \end{bmatrix} = \begin{bmatrix} \dot{\theta}_1 \\ \dot{\theta}_2 \\ \dot{\varphi}_1 \\ \dot{\varphi}_2 \\ \dot{\omega}_{\theta 1} \\ \dot{\omega}_{\theta 2} \\ \dot{\omega}_{\varphi 1} \\ \dot{\omega}_{\varphi 2} \end{bmatrix} = \begin{bmatrix} \omega_{\theta 1} \\ \omega_{\theta 2} \\ \omega_{\varphi 1} \\ \omega_{\varphi 2} \\ \dfrac{4(\varphi_1 - \varphi_2 + \dot{\varphi}_1 - \dot{\varphi}_2 + \tilde{\tau}_1 - \tilde{\tau}_2 - \theta_1 + \theta_2 - \dot{\theta}_1 - \dot{\theta}_2)}{45} \\ \dfrac{4(-\varphi_1 - \dot{\varphi}_1 - \dot{\varphi}_2 - \tilde{\tau}_1 + \dot{\theta}_1 + \dot{\theta}_2)}{45} + \dfrac{89(\varphi_2 + \dot{\varphi}_2 + \tilde{\tau}_2 - \theta_2 - \dot{\theta}_2}{495} \\ \tau_1 - \dot{\varphi}_1 - \varphi_1 + \theta_1 + \dot{\theta}_1 \\ \tau_2 - \dot{\varphi}_2 - \varphi_2 + \theta_2 + \dot{\theta}_2 \end{bmatrix} \quad (1.16)$$

C. PROBLEM FORMULATION FOR RAPID MOTION CONTROL

With all of the relevant system dynamics for the flexible two-link manipulator described mathematically, an optimal control problem formulation to illustrate the new approach for rapid motion control of the links can be developed. The scenario chosen for this example is shown in Figure 3 and Figure 4. The maneuver is a simple maneuver from a straight-arm configuration to an "L" configuration, where each link has slewed 90° relative to its antecedent. Since the problem is to move the two-link arm into an L configuration, the problem is named two-link L, or "TL-L." The starting configuration simply has $\theta_1 = \theta_2 = 0°$, and the final configuration has $\theta_1 = 90°$ and $\theta_2 = 90°$.

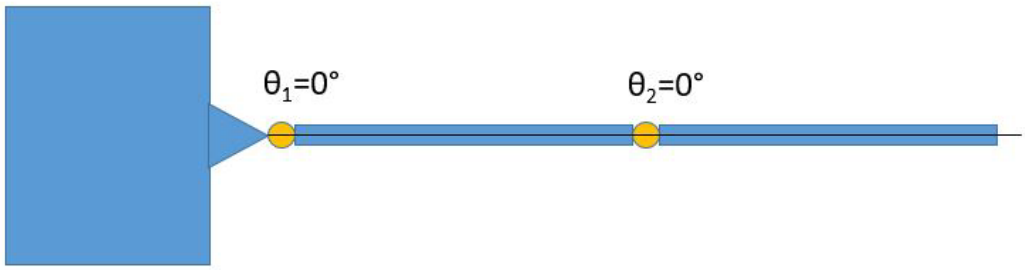

Figure 3. Two-link system in the start (initial) configuration

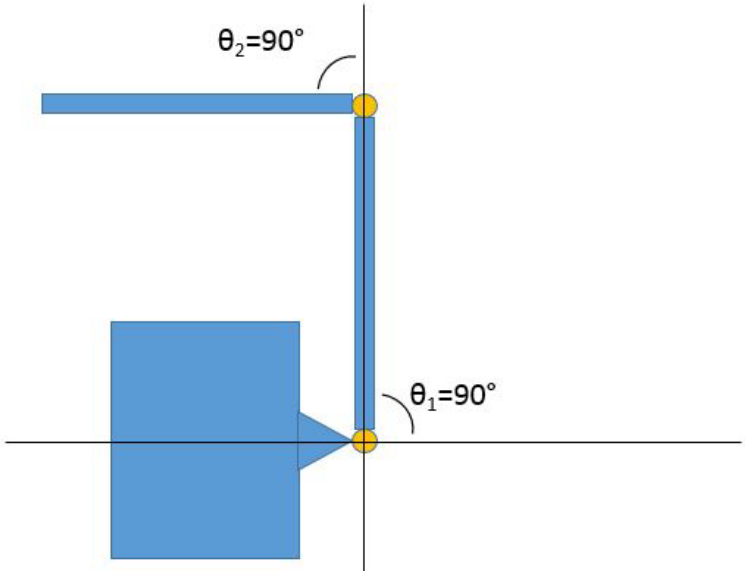

Figure 4. Two-link system in the end (final) “L” configuration

The formulation for the TL-L problem is defined as:

$$
\left.
\begin{gathered}
x = [\underline{\theta}, \underline{\varphi}, \underline{\omega_\theta}, \underline{\omega_\varphi}]^T \in \mathbb{R}^8, u = [\underline{\tilde{\tau}}, \underline{\tau}] \in \mathbb{R}^4 \\
\textit{Minimize} \quad J[x(\cdot), u(\cdot), t_f] = t_f \\
\textit{Subject to} \quad \dot{\theta}_1 = \omega_{\theta_1} \\
\dot{\theta}_2 = \omega_{\theta_2} \\
\dot{\varphi}_1 = \omega_{\varphi_1} \\
\dot{\varphi}_2 = \omega_{\varphi_2} \\
\dot{\omega}_{\theta_1} = \frac{4(\varphi_1 - \varphi_2 + \omega_{\varphi_1} - \omega_{\varphi_2} + \tilde{\tau}_1 - \tilde{\tau}_2 - \theta_1 + \theta_2 - \omega_{\theta_1} + \omega_{\theta_2})}{45} \\
\dot{\omega}_{\theta_2} = \frac{4(-\varphi_1 - \omega_{\varphi_1} - \omega_{\varphi_2} - \tilde{\tau}_1 + \theta_1 + \omega_{\theta_1} + \omega_{\theta_2})}{45} + \frac{89(\varphi_2 + \omega_{\varphi_2} + \tilde{\tau}_2 - \theta_2 + \omega_{\theta_2})}{495} \\
\dot{\omega}_{\varphi_1} = \tau_1 + (\theta_1 - \varphi_1) + (\omega_{\theta_1} - \omega_{\varphi_1}) \\
\dot{\omega}_{\varphi_2} = \tau_2 + (\theta_2 - \varphi_2) + (\omega_{\theta_2} - \omega_{\varphi_2}) \\
(\theta_{1_0}, \theta_{2_0}, \varphi_{1_0}, \varphi_{2_0}) = (0,0,0,0) \\
(\dot{\theta}_{1_0}, \dot{\theta}_{2_0}, \dot{\varphi}_{1_0}, \dot{\varphi}_{2_0}) = (0,0,0,0) \\
(\theta_{1_f}, \theta_{2_f}, \varphi_{1_f}, \varphi_{2_f}) = \left(\pi/2, \pi/2, 0, 0\right) \\
(\dot{\theta}_{1_f}, \dot{\theta}_{2_f}, \dot{\varphi}_{1_f}, \dot{\varphi}_{2_f}) = (0,0,0,0) \\
h_2(t) = 0 \\
h_1(t) = 0 \\
-30 \le \tau_1 \le 30 \\
-30 \le \tau_2 \le 30
\end{gathered}
\right\}, \qquad (1.17)
$$

where

$$
\begin{aligned}
h_1 &= -2m_2 d_1 d_2 \cos(\theta_2)\ddot{\theta}_1 - m_2 d_1 l_2 \cos(\theta_2)\ddot{\theta}_2 - 2m_2 l_1 l_2 \sin(\theta_2)\dot{\theta}_2\dot{\theta}_1 + m_2 l_1 l_2 \sin(\theta_2)\dot{\theta}_2^2 - \tilde{\tau}_1 \\
h_2 &= -m_2 d_1 l_2 \cos(\theta_2)\ddot{\theta}_1 - m_2 l_1 l_2 \sin(\theta_2)\dot{\theta}_1^2 - \tilde{\tau}_2
\end{aligned}
. \qquad (1.18)
$$

The problem formulation shows that the initial system state has the links at 0°, with no rotation on the rotors and no motion for either the links or the rotors. The final orientation will be the “L” configuration described above, with no angular displacement of the rotors and all other elements at rest. Hence, it is desired to perform the maneuver in such a way that there is no residual vibrational energy at the end of the maneuver.

This problem formulation is well defined and easily solved using DIDO, a software tool for solving optimal control problems [13]. However, before coding can take place a precise understanding of the actual problem to be solved must be achieved. Pontryagin's Principle can guide the required analysis.

The first step in applying Pontryagin's Principle is writing the control Hamiltonian:

$$H(\lambda, x, u, t) = F(x, u, t) + \lambda^T f(x, u, t). \tag{1.19}$$

In (1.19), F is the running cost, which, since the problem is looking for the minimum time solution, does not appear in this problem, and **f**(**x**,**u**,t) are the dynamics shown in (1.16). The vector **λ** is covectors related to the states.

Adding path constraints requires the use of the Lagrangian of the Hamiltonian:

$$\bar{H}(\mu, \lambda, x, u, t) = H(\lambda, x, u, t) + \mu^T h(x, u, t). \tag{1.20}$$

The Lagrangian of the Hamiltonian for the rapid maneuver problem is:

$$\begin{aligned}
\bar{H} &= \lambda_{\theta_1}\omega_{\theta_1} + \lambda_{\theta_2}\omega_{\theta_2} + \lambda_{\varphi_1}\omega_{\varphi_1} + \lambda_{\varphi_2}\omega_{\varphi_2} \\
&+ \lambda_{\omega_{\theta_1}}\left[\frac{4(\varphi_1 - \varphi_2 + \omega_{\varphi_1} - \omega_{\varphi_2} + \tilde{\tau}_1 - \tilde{\tau}_2 - \theta_1 + \theta_2 - \omega_{\theta_1} + \omega_{\theta_2})}{45}\right] \\
&+ \lambda_{\omega_{\theta_2}}\left[\frac{4(-\varphi_1 - \omega_{\varphi_1} - \omega_{\varphi_2} - \tilde{\tau}_1 + \theta_1 + \omega_{\theta_1} + \omega_{\theta_2})}{45} + \frac{89(\varphi_2 + \omega_{\varphi_2} + \tilde{\tau}_2 - \theta_2 + \omega_{\theta_2})}{495}\right], \\
&+ \lambda_{\omega_{\varphi_1}}\left(\tau_1 + (\theta_1 - \varphi_1) + (\omega_{\theta_1} - \omega_{\varphi_1})\right) \\
&+ \lambda_{\omega_{\varphi_2}}\left(\tau_2 + (\theta_2 - \varphi_2) + (\omega_{\theta_2} - \omega_{\varphi_2})\right) + \mu_1 h_1 + \mu_2 h_2
\end{aligned} \tag{1.21}$$

where the μ vector is the covector associated with the path constraints.

The Karush-Kuhn-Tucker (KKT) conditions are used to analyze the behavior of the path covectors. Specifically, the complementarity condition shown in (1.22) describes how the values of the μ covectors depend on the values of the path constraint equation.

$$\mu_i \begin{cases} \geq 0 \quad if \quad h_i = h_i^U \\ = 0 \quad if \quad h_i^L \leq 0 \leq h_i^U \\ \leq 0 \quad if \quad h_i = h_i^L \end{cases} \tag{1.22}$$

An example is shown in (1.23) for the first path constraint, h_1.

$$\mu_1 \begin{cases} \geq 0 & if \quad h_1 = 0 \\ = 0 & if \quad 0 \leq h_1 \leq 0 \\ \leq 0 & if \quad h_1 = 0 \end{cases} \tag{1.23}$$

Since in the rapid maneuver problem h_1 is always constrained to be zero, which is both the upper and lower bound, μ_1 is free to take on any value for all times.

To aid in analysis, adjoint equations can be derived from the Lagrangian of the Hamiltonian according to (1.24).

$$-\dot{\lambda} = \frac{\delta \bar{H}}{\delta x} \tag{1.24}$$

These adjoint equations can be useful for verifying whether a solution adheres to the necessary conditions for optimality. However, since in this problem each adjoint equation is a linear combination of several covectors, the expected behavior is difficult to interpret. One example of an adjoint equation is given in (1.25), but all eight are similar.

$$\dot{\lambda}_{\theta_2} = \frac{89}{495}\lambda_{\omega_{\theta_2}} - \frac{4}{45}\lambda_{\omega_{\theta_1}} - \lambda_{\omega_{\varphi 2}} \tag{1.25}$$

One further step in applying Pontryagin's Principle is using the Terminal Transversality Condition to find boundary conditions for covectors. This step is used when there are missing boundary conditions on the states. All boundary values are known for the states, so there is no need to perform transversality analysis as no additional insight into the problem solution will be obtained.

Since the rapid maneuver problem is a minimum time problem, the Hamiltonian value condition shows that the value of the lower Hamiltonian at the final time should be -1 [13]. That is:

$$H\left[@\, t_f\right] = -1. \tag{1.26}$$

Further, the Hamiltonian evolution equation holds that the slope of the Hamiltonian should be zero, since the Hamiltonian is not dependent on time:

$$\frac{\delta H}{\delta t} = 0. \tag{1.27}$$

Combining the Hamiltonian value condition and the Hamiltonian evolution equation results in the necessary condition that the lower Hamiltonian be -1 for all time, for a minimum time problem.

Since this problem seeks the minimum time solution, a bang-bang profile would normally be expected. The result is something different. At the beginning and end of the maneuver the joints experience the maximum torques, but most of the maneuver is accomplished well within the torque limits. This behavior is utilized to control the dynamic coupling between the joints. The maneuver duration was 8.0086 seconds. The control torques are shown in Figure 5.

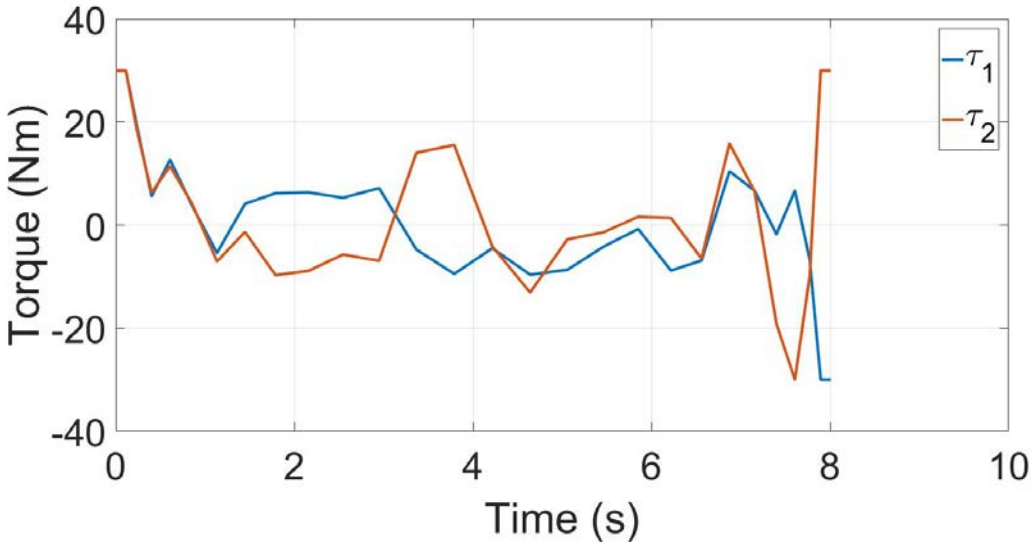

Figure 5. Torque profile for two-link rapid maneuver

Figure 6 shows that the links did in fact achieve the desired final orientation. Link 1 goes to 90°, and link 2 goes to 180°.

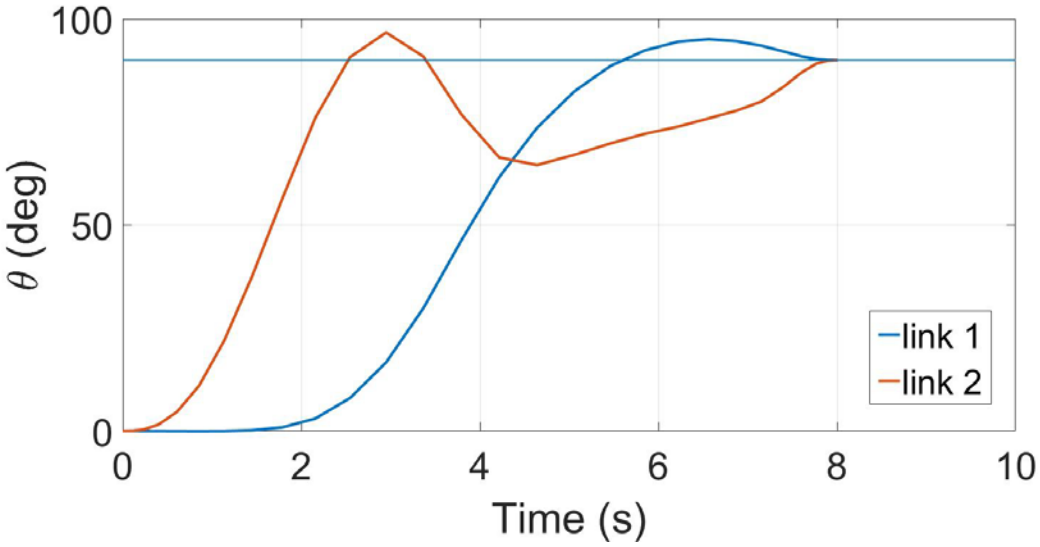

Figure 6. Link angles for two-link rapid maneuver

As specified in the problem description, the links start and end with zero velocity, as shown in Figure 7.

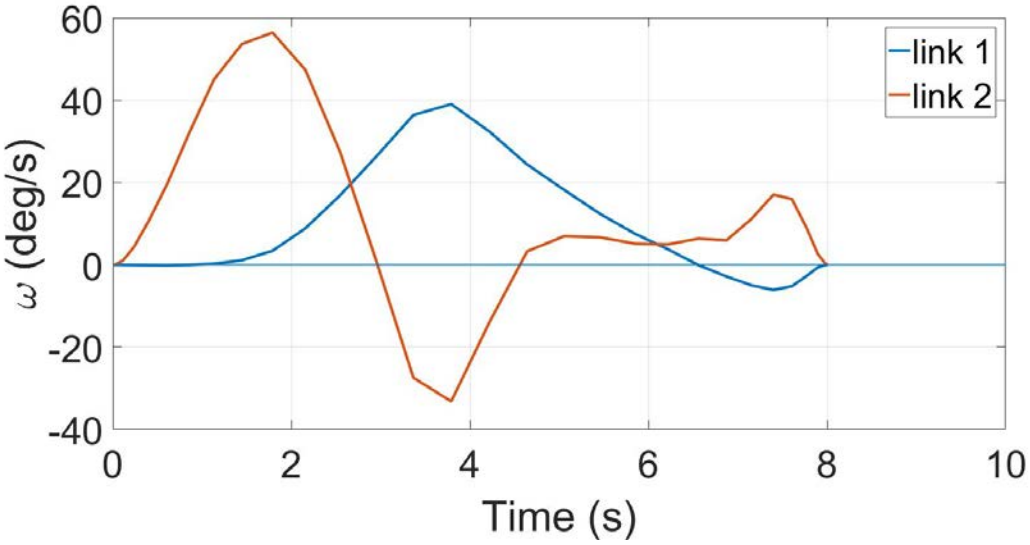

Figure 7. Link angular velocity for two-link rapid maneuver

D. ANALYSIS OF PROOF-OF-CONCEPT RESULTS

While Figure 6 and Figure 7 show the desired result, this must be confirmed through verification and validation. Several checks were performed to verify that the result was the optimal solution. The first test was verifying the feasibility of the result by interpolating the torque trajectories and propagating them through the dynamics. The results of this test are shown in Figure 8 and Figure 9, and were quite successful, as can be measured by how closely the propagated result data points lie over the results from DIDO. The curves are nearly identical.

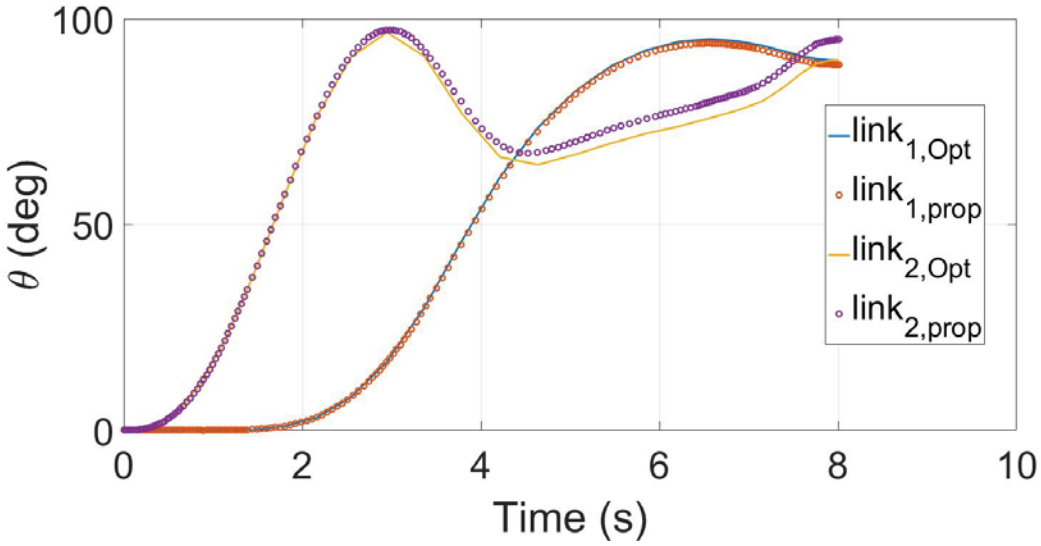

Figure 8. Feasibility test of link angles for two-link rapid maneuver

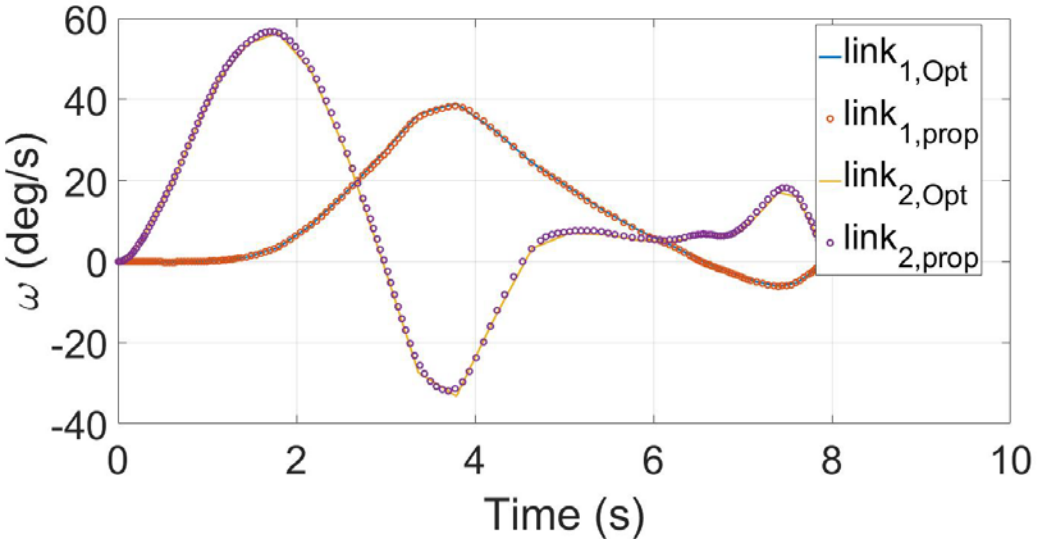

Figure 9. Feasibility test of link angular velocity for two-link rapid maneuver

As discussed above, the Hamiltonian should have a constant value of -1. Figure 10 shows the Hamiltonian is not quite -1, but is nearly there. The mean value is -1.0556 with a standard deviation of 0.1262. The closeness of this result to the expected value of -1 increases confidence that a minimum time solution has been found.

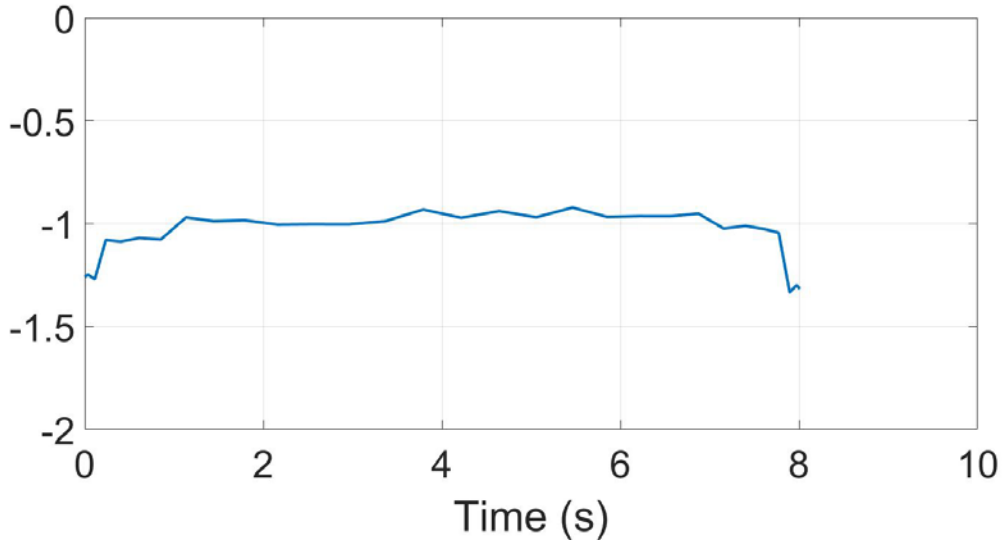

Figure 10. Plot of the Hamiltonian for two-link rapid maneuver

The path constraints, which are the nonlinearities or the virtual torques, can be examined, but they are of limited utility for showing optimality. Since h_1 and h_2 are constrained to be zero at all times, this leaves the corresponding covectors free to take on any value. This is the observed behavior, as shown in Figure 11 and Figure 12.

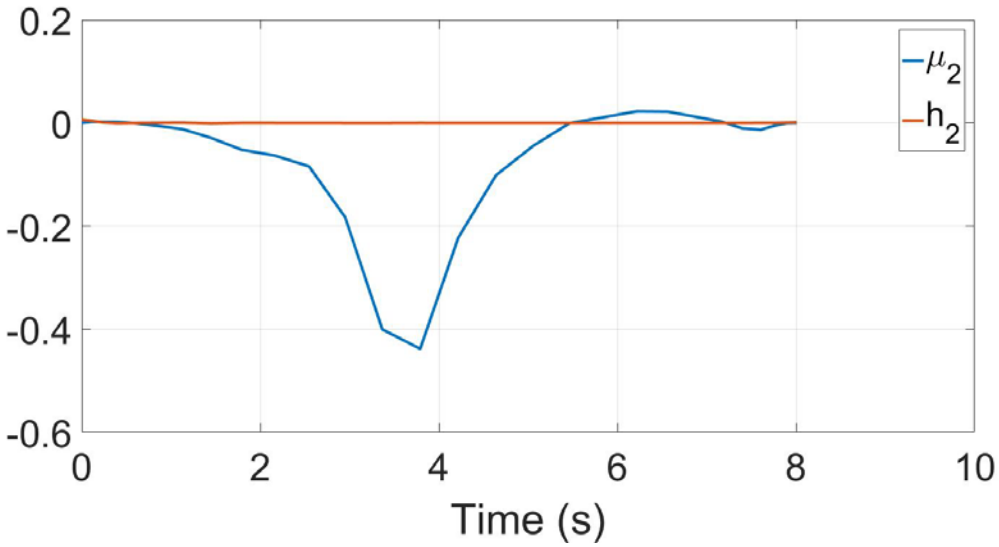

Figure 11. Path constraint 1 on nonlinearities and related covector during two-link rapid maneuver

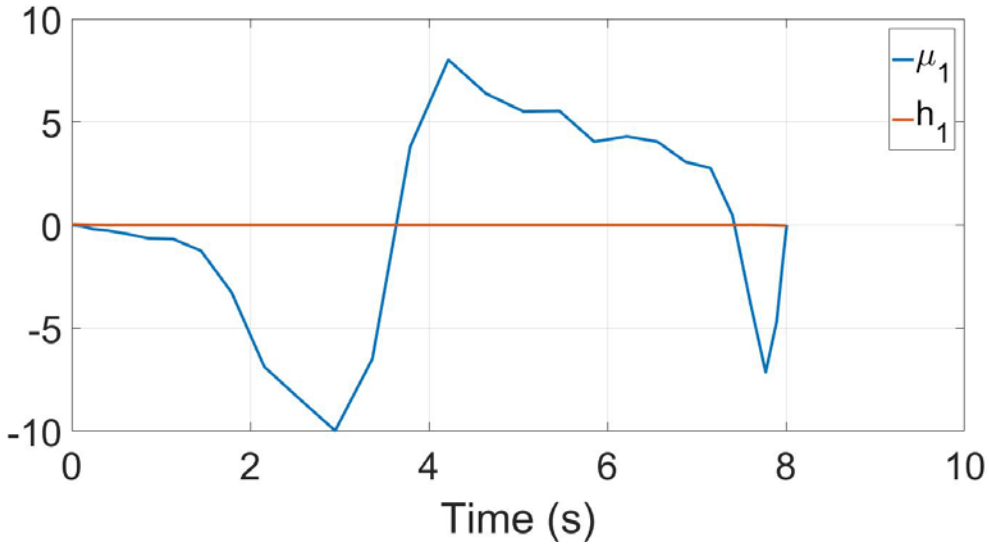

Figure 12. Path constraint 2 on nonlinearities and related covector during two-link rapid maneuver

E. CHAPTER SUMMARY

This chapter began with deriving a dynamical model of a generic multi-body system. This model was then adapted to an idealized version of a robotic arm produced during a previous thesis effort. A sample maneuver was evaluated, and the proper mathematics was used to determine that a rapid maneuver of a flexible two-link system is feasible with the idealized parameters. Since the maneuver is feasible, the model developed in this chapter will be adapted to a real system, and the problem re-solved so that experimental results can be obtained. This process will be discussed in Chapter V. First, however, the experimental system will be described.

THIS PAGE INTENTIONALLY LEFT BLANK

III. MULTI-BODY FLEXIBLE SPACECRAFT SIMULATOR TESTBED

In order to experimentally test the concept described in Chapter II, a multi-body flexible spacecraft simulator (MBSS) testbed was developed and constructed. This testbed was modified and enhanced from a previous iteration completed by Griggs [10], shown in Figure 13. Most components were manufactured at the Naval Postgraduate School, using the machine shop for all aluminum pieces and the Rapid Prototyping Center for all 3D printed components. All electronics were procured as commercial-off-the-shelf parts.

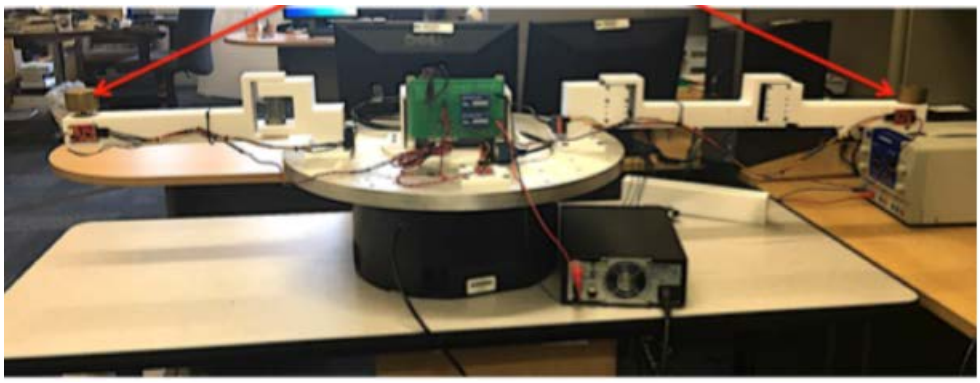

Figure 13. Multi-body flexible spacecraft simulator first iteration. Source: [12].

A. UPDATED TESTBED OVERVIEW

The upgraded testbed is composed of two aluminum disks, 0.6096m (24 inches) in diameter, mounted one over the other with a 0.3048m (12 inches) clearance. Aluminum stanchions are used to support the upper disk. The lower disk is mounted to a single degree of freedom air bearing, and contains most of the electronics. A battery and power distribution system are mounted towards the outside, while a National Instruments cRIO (compact Reconfigurable Input/Output) microcontroller is mounted in the center. The cRIO is Wi-Fi-enabled so that data can be acquired and commands can be sent to the testbed without any wires imparting external torques on the system.

The upper disk holds all of the moving parts, including a rigid/flexible two-link robotic arm, the passive flexible appendage, and the reaction wheel momentum control assembly. A rigid robotic arm composed of an aluminum base and two links, with Dynamixel Pro M42 actuators powering each link, was designed for the testbed. However, a second robotic arm with flexible joints was also procured for the testbed and this latter setup was used for most of this thesis. Both arms can be fitted to the testbed for experimentation. The flexible appendage is 3D printed ABS, with linear extension springs to provide a restoring force. The reaction wheel assembly makes use of Maxon EC flat brushless DC motors as reaction wheels. These are controlled by Maxon EPOS motor controllers. All components and sensors are connected with cables to the cRIO on the bottom deck. Figure 14 is a side view of the MBSS with all components identified in Table 3.

Table 3. Listing of the MBSS components

Component	Description
1	Air bearing
2	Aluminum base plate
3	Aluminum stanchion
4	Aluminum second deck
5	Reaction wheel base
6	Reaction wheel
7	Reaction wheel controllers
8	Rigid/flexible arm
9	Passive appendage base
10	Passive appendage link
11	Extension spring
12	24 V battery
13	National Instruments cRIO controller

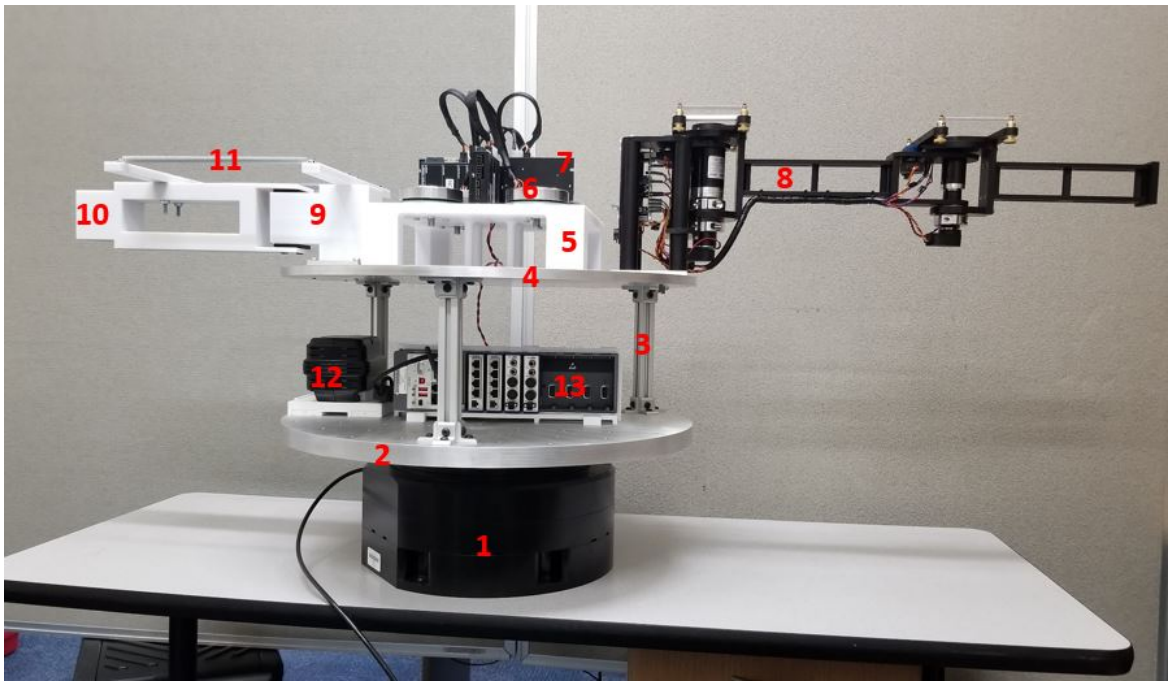

Components are identified in Table 1

Figure 14. Multi-body flexible spacecraft simulator

B. TESTBED CONSTRUCTION

The testbed was developed and built at NPS, taking advantage of the on-site machine shop for metal components and Rapid Prototyping Center for 3D printed parts. A detailed description of each of the testbed components follows.

1. Passive Flexible Appendage

The flexible appendage is a 3D-printed arm consisting of a base, a link, bearings, and springs. This arm is designed to mimic a flexible appendage like an antenna, such as would typically be mounted on a satellite, and the spring mounts allow for simulating varying stiffness effects. The base connects to the MBSS top plate using an aluminum adapter, which is simply an aluminum plate with two sets of four holes. One set of countersunk holes aligns with threaded holes in the flexible arm base and allows the adapter plate to be screwed to the base. The other set of holes allows the adapter plate to be fastened to the MBSS top plate.

The base and link are designed to be modular and expandable. The link features a male and female end, with the male end fitting into the base. This design allows additional passive links to be added, if desired. The top of the link has two parallel hole patterns extending along its length, which allows the springs to be positioned at regular intervals to adjust the flexible response, and also allows for springs to connect to an additional link if that is desired. The flexible appendage was designed using Siemens NX software and printed at the Rapid Prototyping Center at NPS. It is shown in Figure 15.

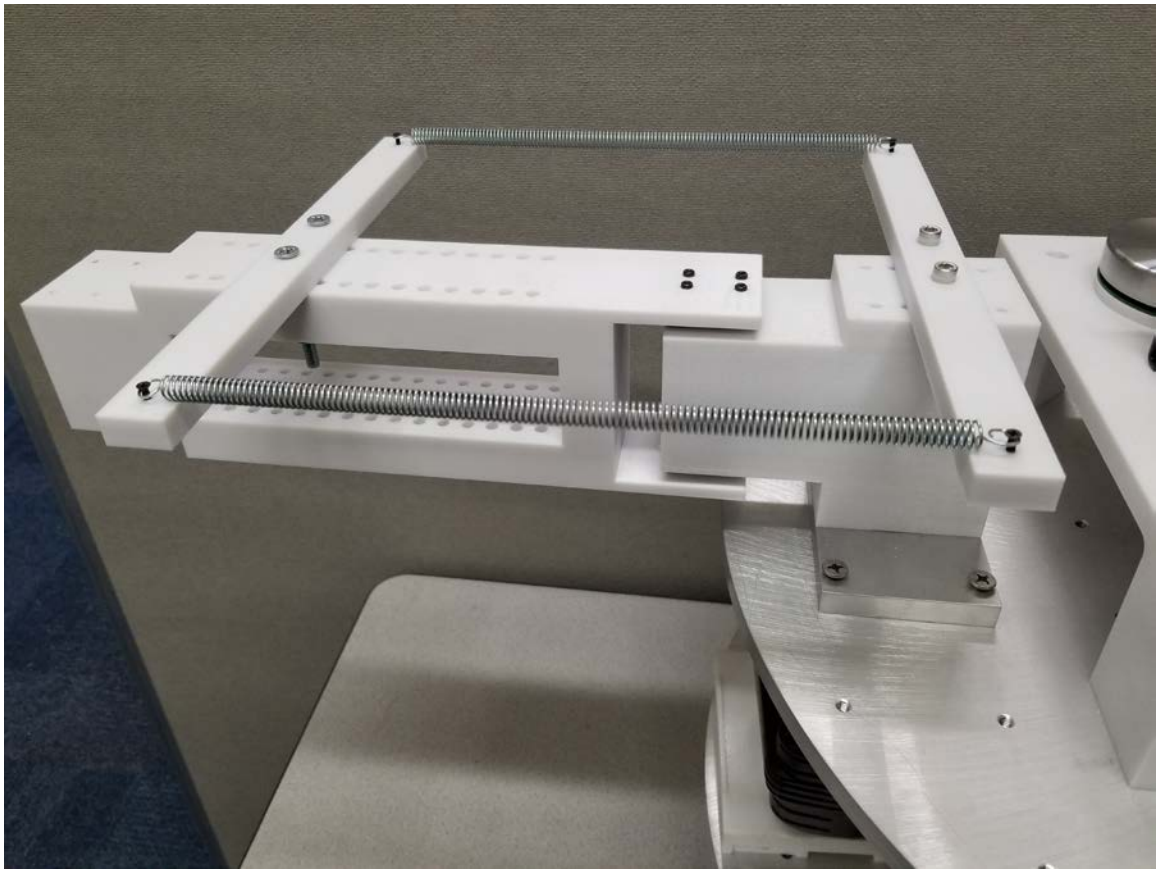

Figure 15. Passive flexible appendage designed and manufactured at NPS

2. Two-Link Rigid Robot Arm

The two-link rigid robotic arm was designed at NPS, and consists of two aluminum links connected to an aluminum base. The base connects to the MBSS top plate in a similar manner as the flexible appendage. Each link is actuated with a Dynamixel Pro MX42 motor [14]. This design was developed by Griggs in his thesis [10] and was manufactured in aluminum for this thesis (see Figure 16). It was determined that a robotic arm with a flexible joint option would be a useful addition moving forward, to allow testing of optimal control theory in application to a flexible structure. To this end, a Quanser 2-degree-of-freedom serial flexible joint (2DOFSFJ) robot was procured. Due to the complexity of the 2DOFSFJ, Chapter IV is devoted to describing this subsystem, its integration, and checkout.

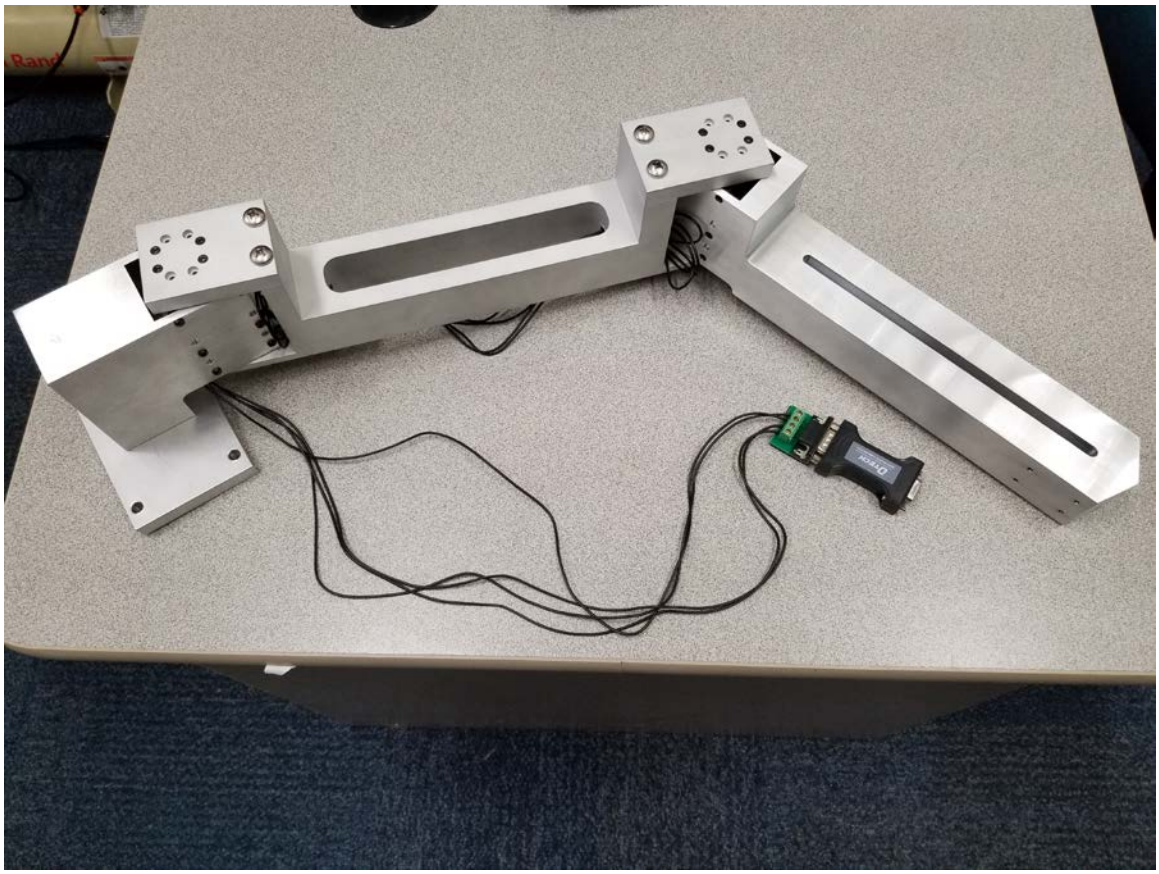

Figure 16. Two-link rigid robotic arm designed and manufactured at NPS

3. Reaction Wheel Momentum Control System

Most large modern satellites are 3-axis stabilized using some sort of momentum control system (MCS). As a result, the MCS can be used to help manage the effects of appendage motion in a passive cooperative fashion. The most common MCS is a reaction wheel array. Reaction wheels operate on the principal that a change in angular momentum imparts a torque on the system.

Although only three reaction wheels are needed to control motion about three axes, it is typical for satellites to have four reaction wheels for the sake of reliability. For the experiment, Maxon EC flat brushless DC motors are used as reaction wheels, as they are cost-effective commercial-off-the-shelf hardware. However, since the DC motors are not specifically designed for this task, they have a smaller momentum storage capacity than a typical reaction wheel [15]. Thus, the MBSS wheels are all arranged so that their torque axis is parallel to the air bearing axis of rotation, as shown in Figure 17. Pending successful trials in this configuration, they can be fit on a new mount to allow torque about all three axes. These four wheels can be arranged in several different configurations, although a pyramidal arrangement is the most popular [16]. The motors are controlled by individual Maxon EPOS controllers.

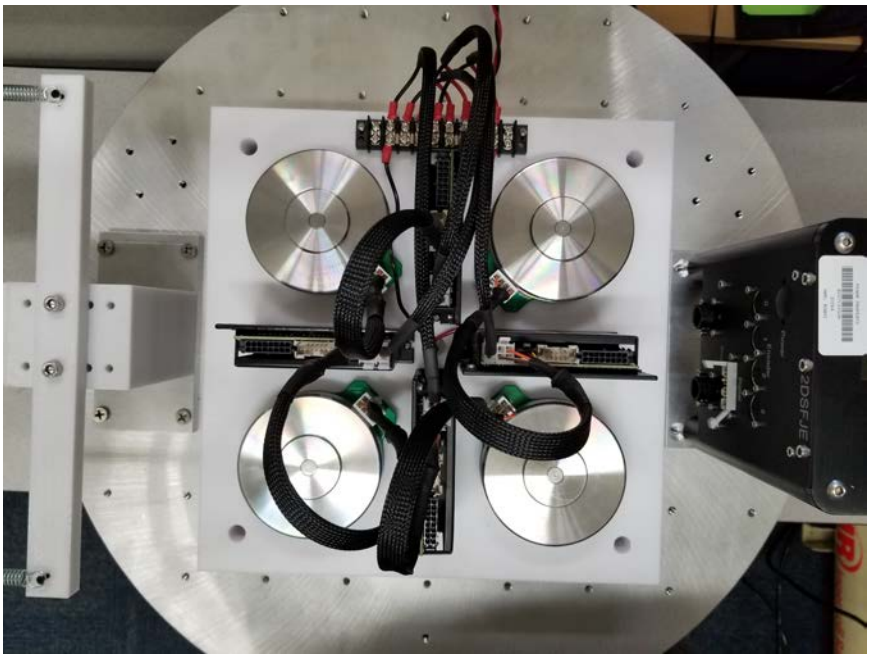

Figure 17. Testbed reaction wheel assembly

4. Flight Control System

The various components of the testbed are in need of a system to both send commands and acquire data. To accomplish both of these tasks, a National Instruments cRIO (compact Reconfigurable Input/Output) embedded controller is used [17]. This unit features Wi-Fi to allow it to communicate with a ground station computer without any wires. Since the testbed floats on an air bearing, this is a key capability, as the wireless communication eliminates any torques which could be imparted to the testbed with a wired connection.

The cRIO is the central command and control hub of the testbed. It communicates with a ground station computer, where the operator can develop maneuvers or analyze data. It also interfaces with the robotic arm and the reaction wheel array, passing commands and receiving data. There are eight total slots for data acquisition cards, which allow for communication to specific devices. Two of these slots are used for the two-link robotic arm. One slot is used for commanding the reaction wheel array, and one slot is available for data relating to the passive flexible appendage. This allows for expansion of the testbed using the remaining four slots. For instance, the NPS-designed robotic arm

could be added to the testbed for advanced simulations and an Inertial Reference Unit (IRU) can be added to establish attitude telemetry of the base motion. The cRIO is shown in Figure 18.

Figure 18. National Instruments Wi-Fi-enabled cRIO

5. Power Distribution

The electronic components of the testbed are battery-powered to create a stand-alone system. A cordless drill battery is repurposed, providing 24 volts DC. This is sufficient to power the cRIO and the reaction wheel array. Additional power electronics are required for the Quanser 2DOFSFJ robotic arm. For all of the testing in this thesis, the 2DOFSFJ was run with the provided 120 volts AC power system. This was sufficient for stationary testing, but the testbed's power system will require modification to accommodate the 2DOFSFJ when the air bearing is activated and floating maneuvers are executed. The battery, connected to the cRIO and reaction wheel array, is shown in Figure 19.

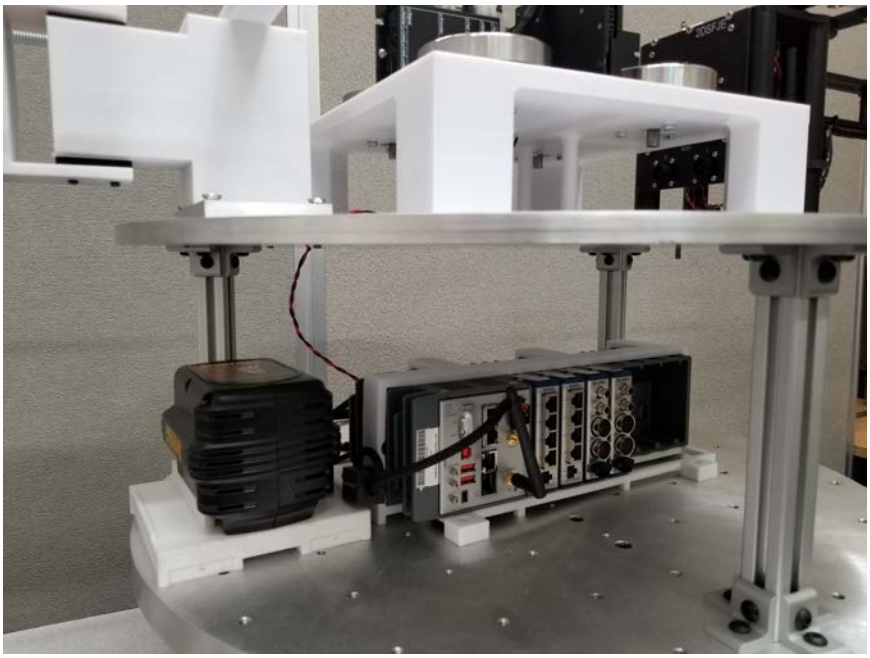

Figure 19. Battery connected to cRIO and reaction wheel array

C. CHAPTER SUMMARY

This chapter examined the current iteration of the Multi-Body Spacecraft Simulator, and all of its components. The MBSS has been built up to provide extensive laboratory capabilities. The ability to rapidly design and test parts using NPS resources has added to the overall state of readiness of the testbed. The redesigned flexible appendage and the reaction wheel array add versatility and capabilities to the system that were previously absent. The battery and Wi-Fi-enabled cRIO will allow the testbed to test more realistic spacecraft maneuvers without the complication of an umbilical.

THIS PAGE INTENTIONALLY LEFT BLANK

IV. TWO-LINK FLEXIBLE JOINT ARM

An additional two-link robotic arm was procured for the testbed to extend its capabilities and allow for more a wider range of experiments. The Quanser 2DOF serial flexible joint (2DOFSFJ) robotic arm was chosen because it has flexible joints that can be tuned depending on requirements [18]. The hardware also came with the Quanser Real-time Control (QUARC) software, which allows the user to program maneuvers easily using MATLAB-Simulink software. QUARC is also compatible with the cRIO platform, making the migration of the results of this thesis to the embedded flight control computer straightforward.

A. OVERVIEW OF 2DSFJ ROBOT CAPABILITIES

The 2DOFSFJ comprises two links, each powered by a DC motor driving a harmonic gearbox with zero backlash. For angular displacement measurement, the motors and flexible joints are equipped with quadrature optical encoders [18]. Each joint has a range of ±90°.

B. INSTALLATION AND INITIAL CHECKOUT

Upon receipt of the equipment, all items were unpacked and inspected for damage. Once all items had been verified, the provided QUARC software was installed on a lab computer. The equipment consists of the arm itself, mounted on a baseplate, a multi-channel linear current amplifier, and a data acquisition unit. The amplifier is needed to power the arm and the data acquisition unit, and this latter part interfaces with the ground station computer via USB cable. The test setup of the 2DOFSFJ is shown in Figure 20. The QUARC had preprogrammed maneuvers, which were useful in learning how to control the arm. The flexible joints were much more flexible than expected, which is good for laboratory experimentation, due to the easily measurable oscillations, and visualization. The design of the flexible joint mechanism allowed for braces to be installed, which effectively made the flexible joint robot into a rigid joint robot. The joints, with 3D printed braces, are shown in Figure 21. The inset is a more detailed image, showing how the brace has two nubs which fit into alternate spring mount holes

on the flexible joint. After verifying that the equipment was in working order and that it was setup correctly, it was turned on and basic commands were sent using MATLAB to verify the signal pathway.

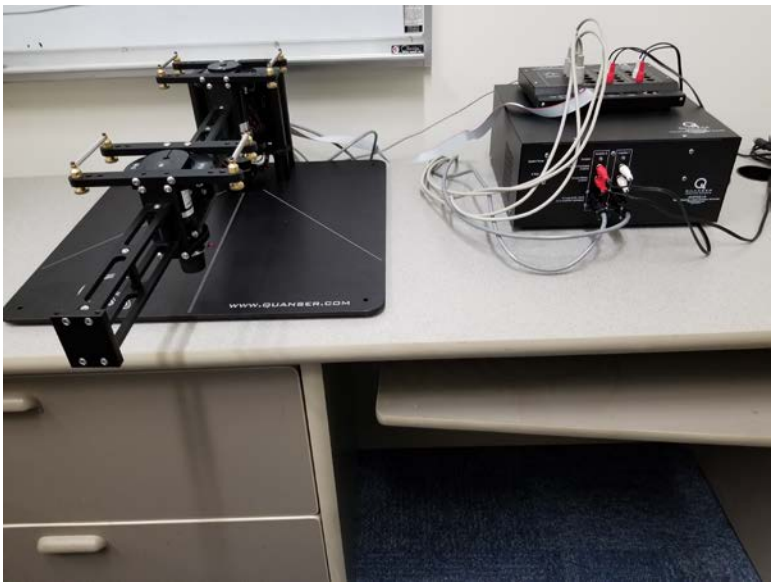

Figure 20. 2DOFSFJ initial setup

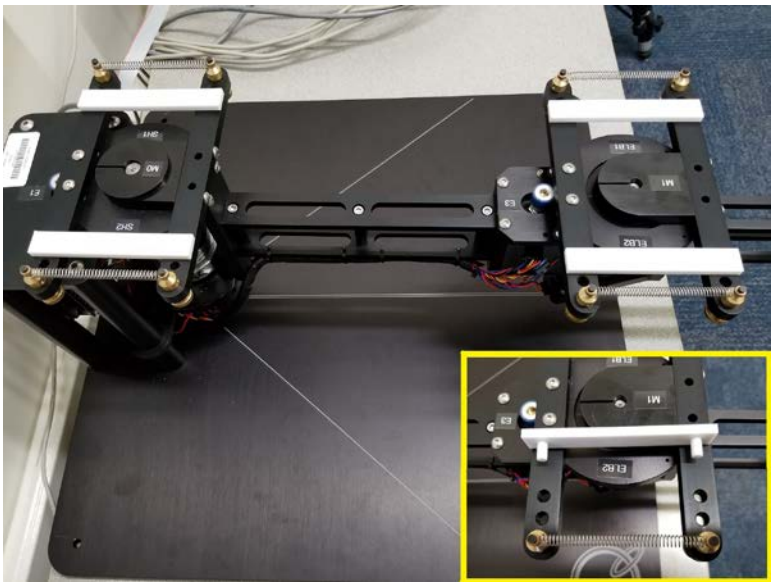

Figure 21. 2DOFSFJ with link braces and brace detail inset

C. VERIFICATION OF COMPONENTS

Before detailed analysis could be completed on the 2DOFSFJ, the joint flexibility had to be determined. This step was important because the mathematical model, which the optimal control maneuver uses, should accurately model the physical properties of the arm. The springs on the flexible joints were not labeled, so the spring constant needed to be determined. This was accomplished via a simple experiment using Hooke's law,

$$F = -kx\,. \tag{1.28}$$

The springs were removed from the 2DOFSJ and the unstretched length measured. Then, the springs were hung from a vice and stretched with known masses. The stretched length was measured, and the results were used to determine the spring constant. The lab setup used to measure the springs is shown in Figure 22.

Figure 22. Measuring the 2DOFSFJ spring constants

Table 4 summarizes the data collected in the spring constant experiment. The springs were attached to brass connectors to facilitate their installation in the 2SOFSFJ joints. These connectors were very difficult to remove, so only one was removed and weighed, and the calculations take into account the mass of the connectors which were not removed. Since the experimental setup clamped one of the brass connectors in a vise, the mass of only one connector was added to the mass of the brass weight for determining the spring constant. A spring with its brass connectors is shown in Figure 23.

Table 4. Spring constant calculation

	Left Elbow	Right Elbow	Left Shoulder	Right Shoulder
Length (m)	0.03175	0.028575	0.041275	0.0523875
Extended length (m)	0.053975	0.0508	0.05715	0.0682625
Displacement (m)	0.022225	0.022225	0.015875	0.015875
Mass of brass connectors (kg)	0.009	0.009	0.009	0.009
Mass with brass connectors (kg)	0.024	0.024	0.025	0.024
Mass without brass connectors (kg)	0.006	0.006	0.007	0.006
Mass of brass weight (kg)	0.492	0.492	0.984	0.984
Adjusted mass of weight (kg)	0.501	0.501	0.993	0.993
Gravity (m/s^2)	9.81	9.81	9.81	9.81
Force (N)	4.91481	4.91481	9.74133	9.74133
Spring constant (N/m)	221.1388	221.138808	613.6270866	613.6270866

Figure 23. Spring with brass connectors

D. INITIAL CHECKOUT AND MODEL VALIDATION

After verifying that the 2DOFSFJ was physically as expected and that it could execute maneuvers, the system dynamic response needed to be characterized. This was done by completing four maneuvers. The system was first operated in an open loop, where each link was given a current for a short time. This was completed with the flexible joints and again with the braces installed for a rigid link response. The second maneuver used a standard PD controller and the links were commanded to travel to a specific orientation. This was also done in the flexible and rigid configurations.

Since the 2SOFSFJ has joint angle limits of -90° to +90°, the experimental maneuver was altered. The shoulder was commanded to +30° and the elbow was commanded to -30°. This allows enough motion to accurately assess the performance of the system.

1. Open-Loop Tests

The open-loop trials demonstrate that the system is responsive to current commands alone.

a. Flexible joint

The current response of the flexible joint configuration of the open-loop trials is shown in Figure 24 and Figure 25. These plots show an error between the commanded and actual currents. The deviation is meant to overcome or compensate for the friction in the joints and is therefore not of concern.

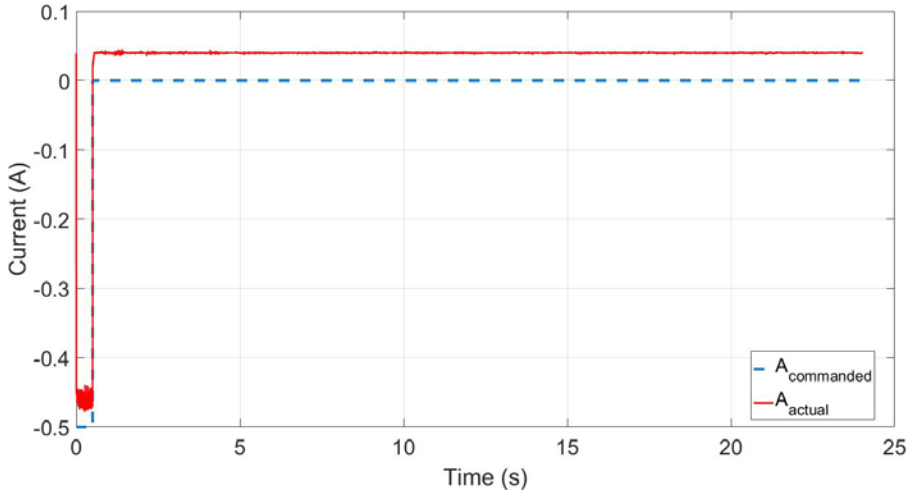

Figure 24. Open loop, flexible joint, shoulder actuator current

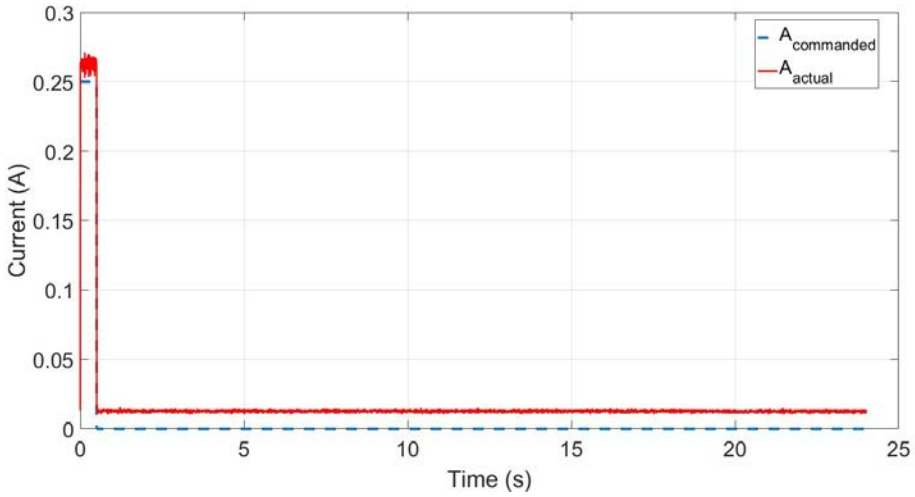

Figure 25. Open loop, flexible joint, elbow actuator current

As shown in Figure 26 and Figure 27, the vibrations induced by the open-loop current pulses last more than 15 seconds. These plots could be used to experimentally deduce the damping coefficients of the shoulder and elbow joints, which would be useful in developing a more accurate mathematical model of the system. However, the parameters supplied by Quanser were determined to be adequate for experiments.

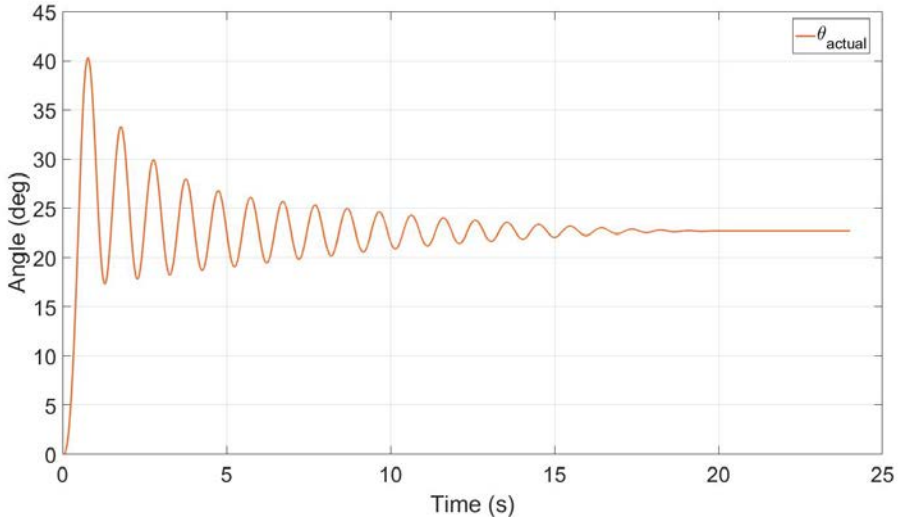

Figure 26. Open loop, flexible joint, shoulder angle response

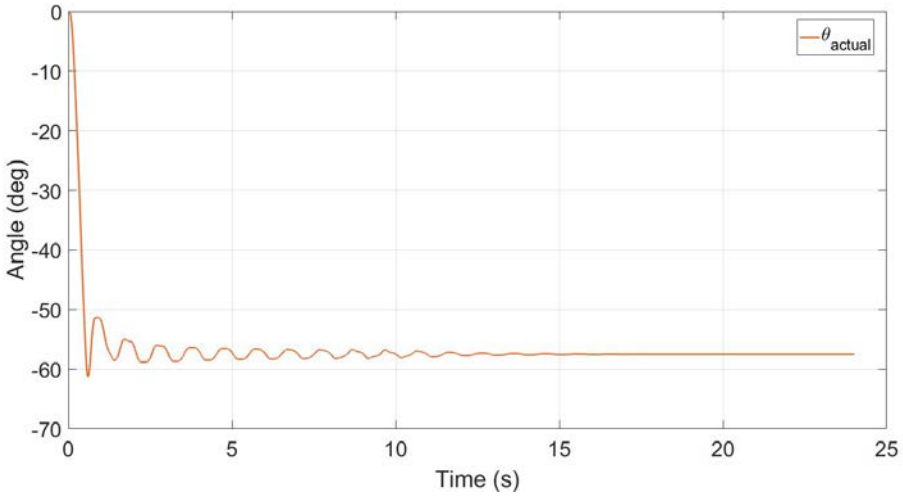

Figure 27. Open loop, flexible joint, elbow angle response

b. Rigid joint

The system was modified for rigid joint motion and the same current profile as the flexible joint version was applied. Because the joint flexibility was removed, however, the response was very different. The response of the shoulder and elbow links, shown in Figure 28 and Figure 29, mimicked a simple double integrator response. The large difference in response between the flexible and rigid joint systems is the main reason why control of flexible systems requires careful attention.

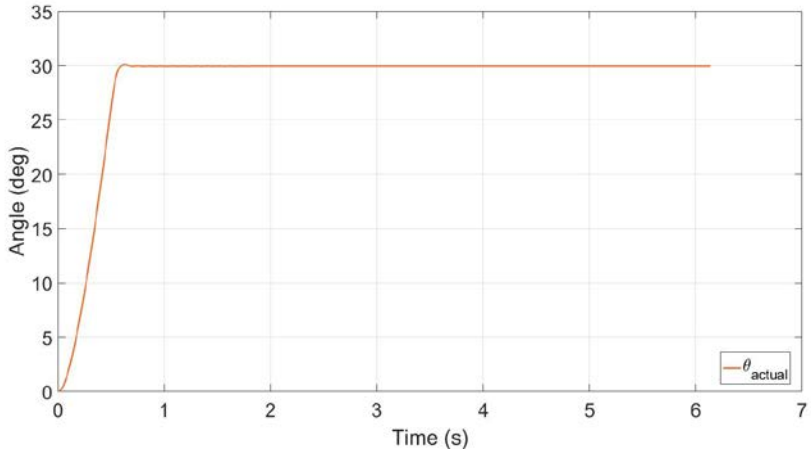

Figure 28. Open loop, rigid joint, shoulder angle position

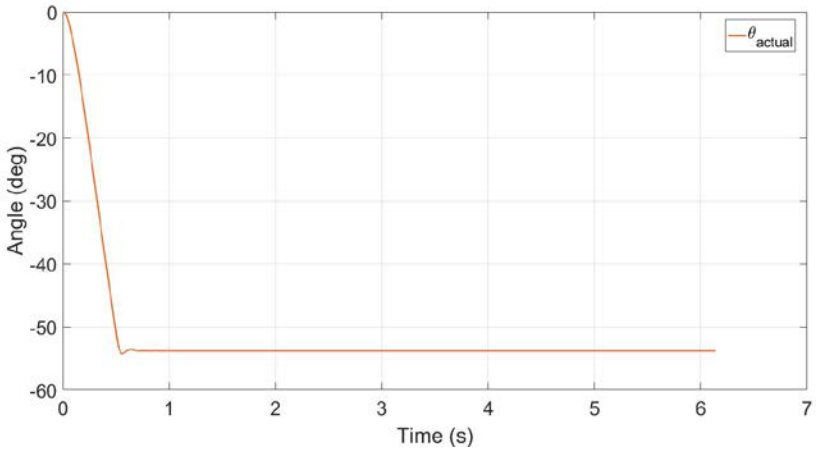

Figure 29. Open loop, rigid joint, elbow angle position

2. Closed-Loop Tests

A maneuver was performed in a closed-loop configuration, where the shaft angular displacement and angular velocity errors were fed back for a partial state feedback loop. This means that the difference between the commanded and actual angular displacement and angular velocities of the shafts are used to adjust the command signal to the actuator. However, there are also encoders on the links in addition to the actuator shafts that can be used for a full-state feedback scheme. Only half of the total available states are used for this control scheme.

a. Flexible joint

The flexible joint response resulted in approximately 1° steady state error (due to friction) for both the shoulder and elbow links, with the induced vibrations ceasing after approximately six seconds, as shown in Figure 30 and Figure 31.

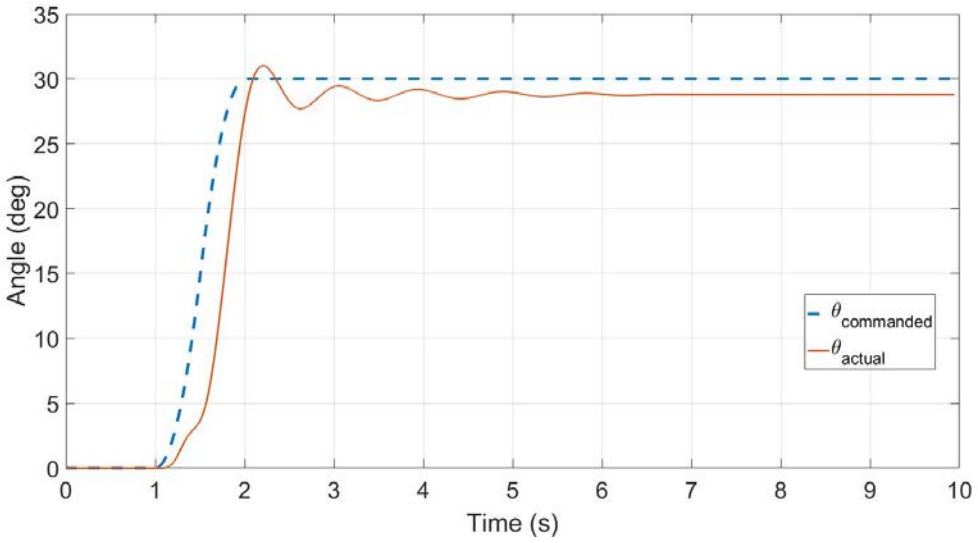

Figure 30. Closed loop, flexible joint, shoulder link angular displacement

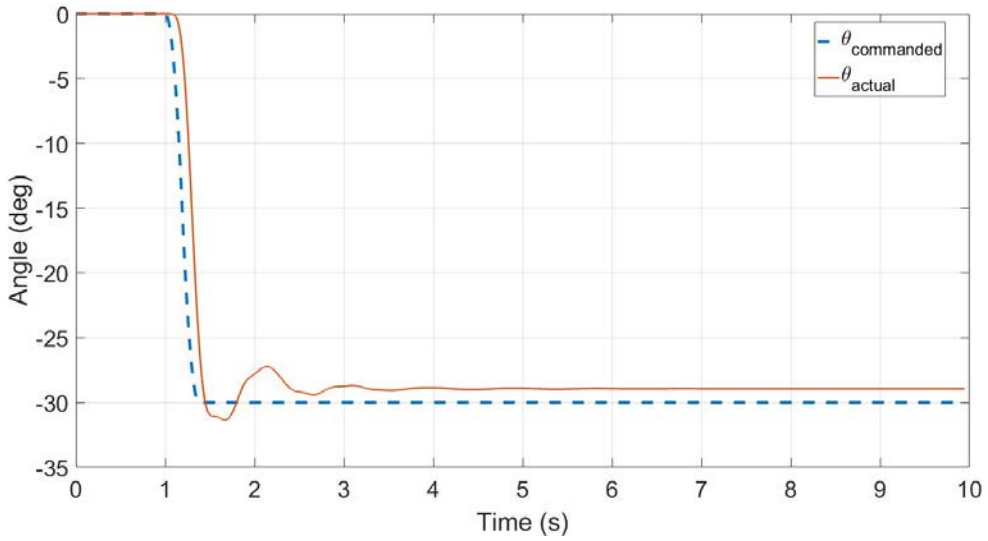

Figure 31. Closed loop, flexible joint, elbow link angular displacement

Table 5 gives a summary of the performance of the closed-loop, flexible joint system. The steady state error is simply the difference between the steady state value achieved measured and the desired angle. The peak-to-peak magnitude of the oscillations measures peak of the first oscillation only. The 2% settling time is based on the actual steady state value, not the desired angle, because no attempt was made to compensate for friction.

Table 5. Closed loop, flexible joint system performance summary

	Shoulder	Elbow
Steady state value	28.78º	-28.95º
Steady state error	1.22º	1.05º
Peak-to-peak magnitude	3.32º	4.12º
2% settling time	3.13 s	2.32 s

b. Rigid joint

The rigid joint maneuver exhibited no overshoot or residual vibrations. Instead, it was very well damped. A 1° steady state error for both the shoulder and elbow links was recorded, as shown in Figure 32 and Figure 33. The error was a result of friction in the joints, as before.

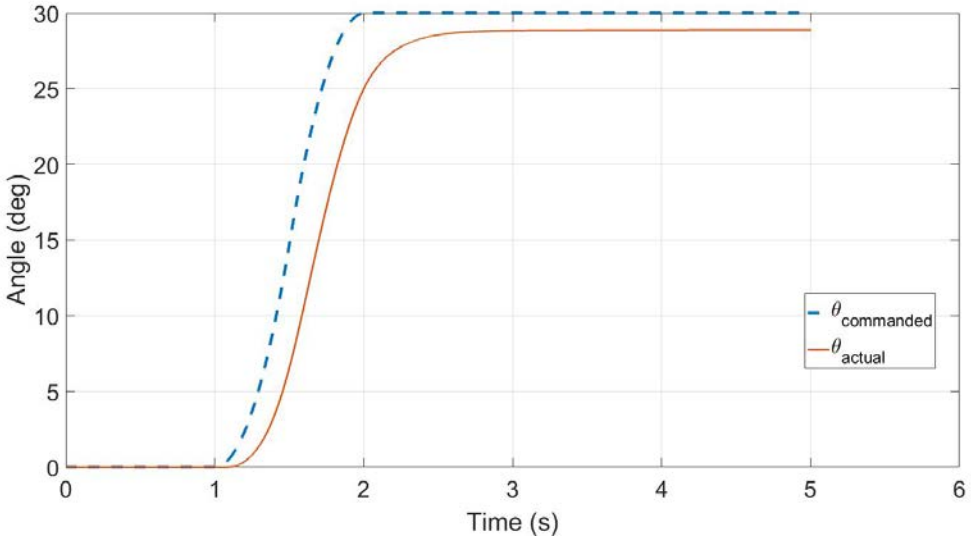

Figure 32. Closed loop, rigid joint, shoulder link angular displacement

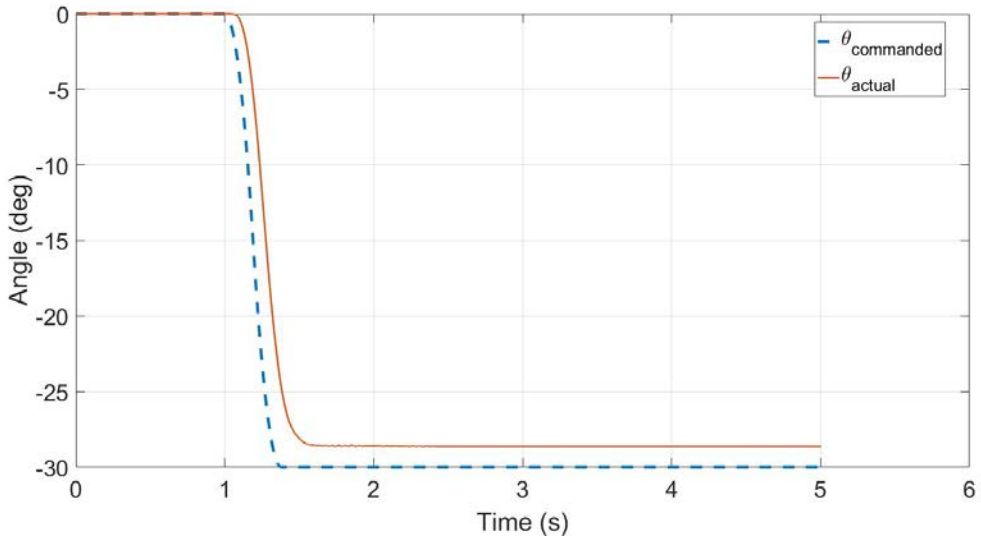

Figure 33. Closed loop, rigid joint, elbow link angular displacement

Table 6 is a summary of the performance metrics for the closed loop, rigid joint experiment.

Table 6. Closed loop, rigid joint system performance summary

	Shoulder	Elbow
Steady state value	28.88º	-28.63º
Steady state error	1.12º	1.37º
Rise time	2.388 s	1.496 s

E. CHAPTER SUMMARY

This chapter described the two-link flexible joint robot arm and its initial checkout. The experiments show that residual vibrations are present for the flexible joint maneuvers. This is because the supplied 2SOFSFJ controller is not specifically designed to control motion-induced vibrations. The closed loop control results in an error in both the shoulder and elbow links for either rigid or flexible joints. This is due to friction, the compensation of which will not be addressed in this thesis.

V. EXPERIMENTAL VERIFICATION OF A RAPID MANEUVER

Based on the results of Chapter II, it appears feasible to execute a minimum-time maneuver on a two link flexible joint system, such that there are no residual vibrations. This chapter details the effort to demonstrate such a maneuver experimentally.

A. MODIFICATION OF MATHEMATICAL MODEL

The mathematical model developed in Chapter II was based on an idealized arm, where the spring rates, damping coefficients, and rotor moment of inertia were the same for each joint. The 2DOFSFJ has different spring rates and damping coefficients for each joint, as well as different actuators to drive the joints. These physical differences require slight reworking the equations to include the new variables. These physical parameters are shown in Table 7.

Table 7. 2DOFSFJ physical parameters

Symbol	Parameter	Value
m_1	Link 1 mass	2.6425 kg
m_2	Link 2 mass	0.87326 kg
d_1	Link 1 distance to COM	0.159 m
d_2	Link 2 distance to COM	0.055 m
I_1	Link 1 MOI	0.0392 kg·m^2
I_2	Link 2 MOI	8.0828x10^{-3} kg·m^2
l_1	Link 1 length	0.343 m
l_2	Link 2 length	0.267 m
c_1	Link 1 damping coefficient	0.0176 N·m·s/rad
c_2	Link 2 damping coefficient	0.028211 N·m·s/rad
k_1	Shoulder spring constant	9.90 N/m
k_2	Elbow spring constant	4.20 N/m
Jr_1	Shoulder rotor MOI	0.0637 kg·m^2
Jr_2	Elbow rotor MOI	3.5059x10^{-3} kg·m^2
dC_1	Shoulder rotor damping coefficient	4.050 N·m·s/rad
dC_2	Elbow rotor damping coefficient	0.125 N·m·s/rad

These new constants were integrated into equation (1.6) and resulted in

$$\begin{bmatrix} m_{11} & m_{12} & 0 & 0 \\ m_{21} & m_{22} & 0 & 0 \\ 0 & 0 & J_{r1} & 0 \\ 0 & 0 & 0 & J_{r2} \end{bmatrix} \begin{bmatrix} \ddot{\theta}_1 \\ \ddot{\theta}_2 \\ \ddot{\varphi}_1 \\ \ddot{\varphi}_2 \end{bmatrix} + \begin{bmatrix} -2r\dot{\theta}_2 + c_1 & -r\dot{\theta}_2 & -c_1 & 0 \\ r\dot{\theta}_1 & c_2 & 0 & -c_2 \\ -dC_1 & 0 & dC_1 & 0 \\ 0 & -dC_2 & 0 & dC_2 \end{bmatrix} \begin{bmatrix} \dot{\theta}_1 \\ \dot{\theta}_2 \\ \dot{\varphi}_1 \\ \dot{\varphi}_2 \end{bmatrix} + \begin{bmatrix} k_1 & 0 & -k_1 & 0 \\ 0 & k_2 & 0 & -k_2 \\ -k_1 & 0 & k_1 & 0 \\ 0 & -k_2 & 0 & k_2 \end{bmatrix} \begin{bmatrix} \theta_1 \\ \theta_2 \\ \varphi_1 \\ \varphi_2 \end{bmatrix} = \begin{bmatrix} 0 \\ 0 \\ \tau_1 \\ \tau_2 \end{bmatrix} \quad (1.29)$$

Other than adding in these constants, the problem formulation remained the same as in Chapter II, and the problem was fortuitously well-scaled. A new minimum-time maneuver was solved using DIDO and the resultant trajectories were then used as the commands for the physical implementation.

B. TESTING THE MANEUVER

The 2DOFSFJ profiled in Chapter IV is a viable platform to perform this maneuver on, except that the allowable joint angles only extend from -90° to +90°. The previously examined maneuver calls for the joints to reach 90°, and any overshoot would exceed the allowable range. Due to this complication, a maneuver over a smaller range was used. The new maneuver, shown in Figure 34, will stay well within the joint limits.

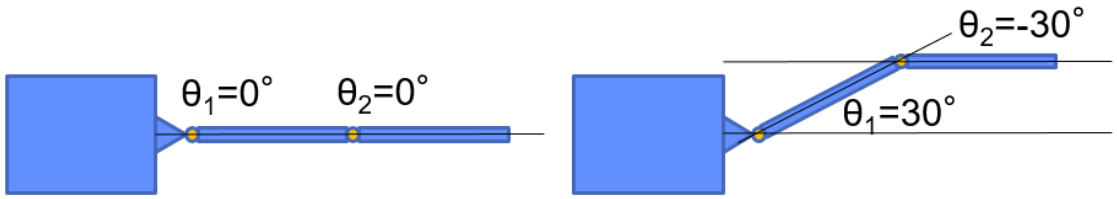

Figure 34. Schematic of 30-degree maneuver for experiments

C. EXPERIMENTAL IMPLEMENTATION

1. Implementation

The performance of the experimental system will be progressively evaluated using a by first implementing a baseline PD controller, then using an open loop with the optimal torque trajectory, then with a closed loop and partial state feedback, and finally with open loop and full-state feedback. These experiments will all make use of the PD controller that was supplied with the QUARC software, but the latter three experiments will feed in the optimal maneuver trajectories. Figure 35 is a representative schematic of the overall control system used for the experiments. The control signals are derived either with a sigmoid function generator, which was used to compute the trajectories for the baseline tests, or using DIDO outputs, which are the optimal maneuver trajectories. The outputs of the signal generator are control signals for the angles or angular rates for the shoulder and elbow links and shafts, as well as the control torques for the joint actuators. In the experiments that were conducted, certain signals were either used in the control system, or terminated, depending on the test. These possible control signals, as well as the measured states, are labeled in the red boxes.

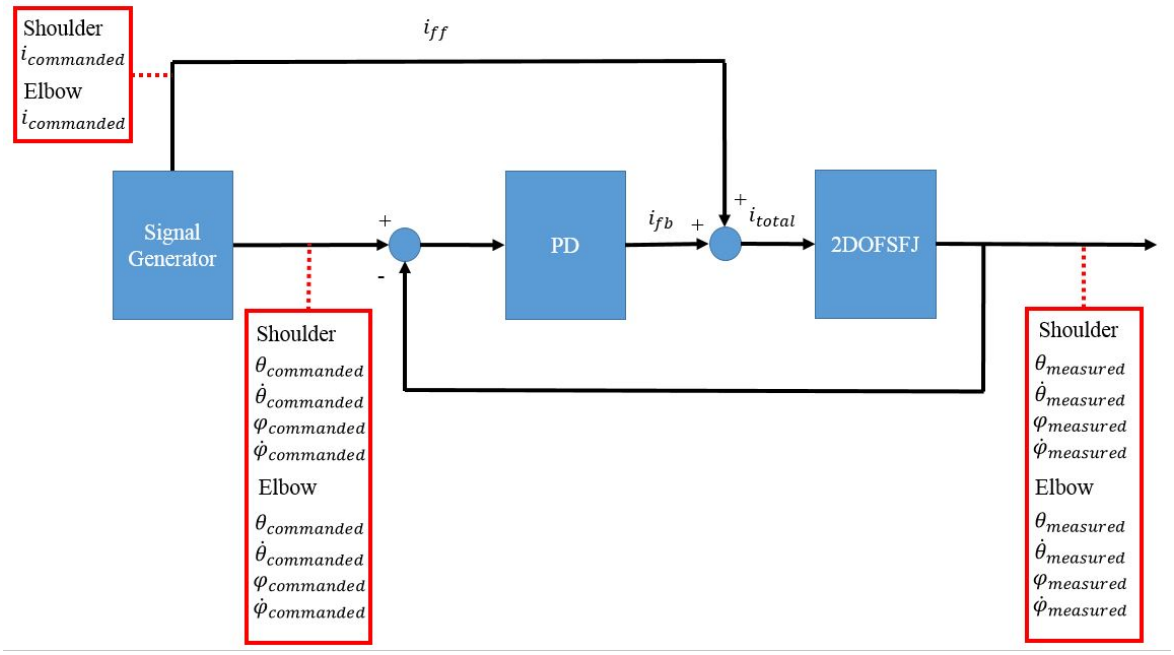

Figure 35. Representative block diagram of control system

The current commands that actuate the joints are a combination of the feedback (fb) and feed forward (ff) currents, as shown in equation (1.30).

$$i_{total} = i_{fb} + i_{ff} \tag{1.30}$$

The feedback currents are the result of gains applied to the difference between the commanded and measured states, as shown in equation (1.31)

$$\begin{aligned} i_{shoulder} &= K_{p_{\theta 1}}\left(\theta_1^* - \theta_1\right) + K_{d_{\theta 1}}\left(\dot{\theta}_1^* - \dot{\theta}_1\right) + K_{p_{\varphi 1}}\left(\varphi_1^* - \varphi_1\right) + K_{d_{\varphi 1}}\left(\dot{\varphi}_1^* - \dot{\varphi}_1\right) \\ i_{elbow} &= K_{p_{\theta 2}}\left(\theta_2^* - \theta_2\right) + K_{d_{\theta 2}}\left(\dot{\theta}_2^* - \dot{\theta}_2\right) + K_{p_{\varphi 2}}\left(\varphi_2^* - \varphi_2\right) + K_{d_{\varphi 2}}\left(\dot{\varphi}_2^* - \dot{\varphi}_2\right) \end{aligned}. \tag{1.31}$$

The starred variables are the commanded states, and the un-starred are the measured states. Variables θ_i refer to the link angles, and φ_i refer to the shaft angles. Equation (1.32) shows how full-state feedback is implemented, but it is easy to adjust these equations for partial state feedback, simply by setting $K_{p\theta}$=$K_{d\theta}$=0. The gain values are LQR gains, tuned to the 2DOFSFJ and set by Quanser in the provided QUARC software.

2. Baseline PD Controller

The first trial that was performed used the control law that came supplied with the QUARC software. Based on the characterization in Chapter IV, this system appears fairly accurate. Since PD controllers are commonly used, this maneuver will be used as a baseline against which to compare the optimal control maneuver. The command signals are the result of a step input being converted to a sigmoid using a QUARC sigmoid generator. This generates trajectories for the shafts only. Since only the shaft angles and angular rates were commanded, the equations in (1.32) were modified to eliminate the link feedback.

The PD controller does a fair job at reaching the commanded positions, as shown in Figure 36 and Figure 37. There is some vibration of the shoulder for more than 5 seconds, but the system stabilizes to a steady state error of approximately 2°. The elbow reaches its desired position faster with only half of the error in position.

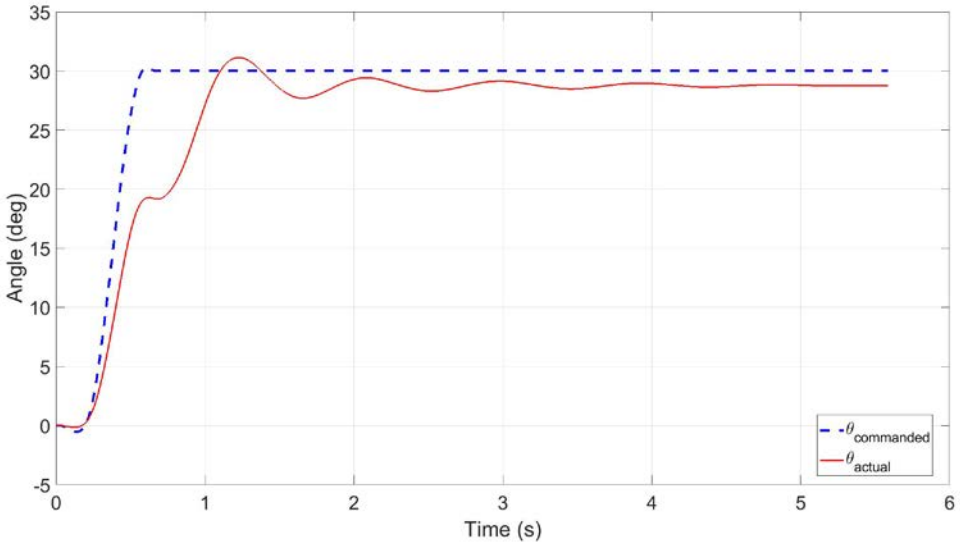

Figure 36. Baseline PD controller response: Shoulder link angular displacement

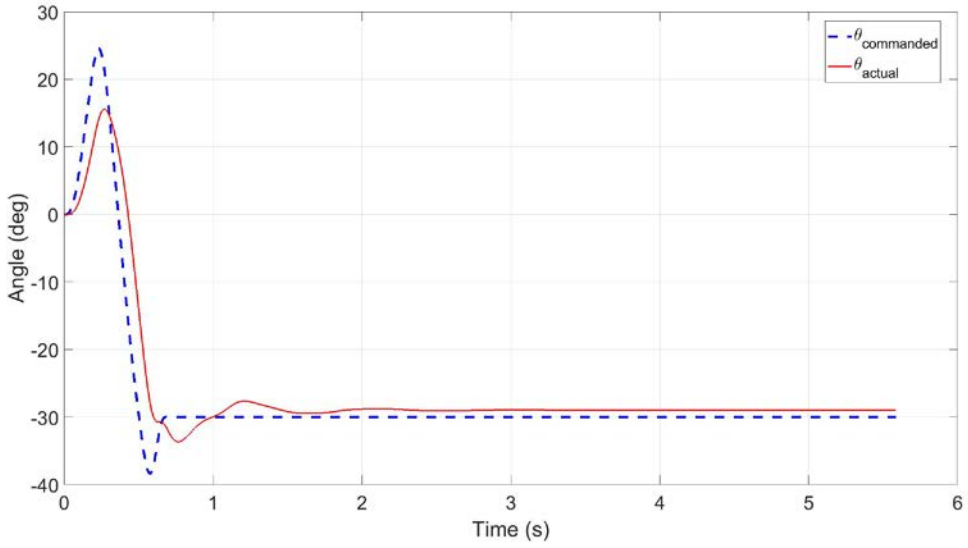

Figure 37. Baseline PD controller response: Elbow link angular displacement

Figure 38 and Figure 39 show the angular velocity of the shoulder and elbow links, respectively. The elbow reaches rest in approximately 2 seconds, while the shoulder continues to oscillate for more than 5 seconds.

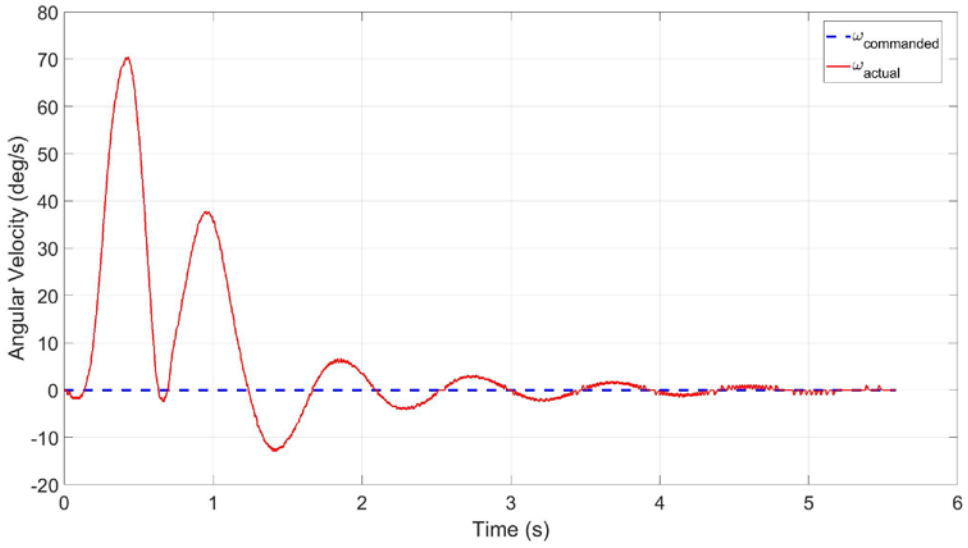

Figure 38. Baseline PD controller response: Shoulder link angular velocity

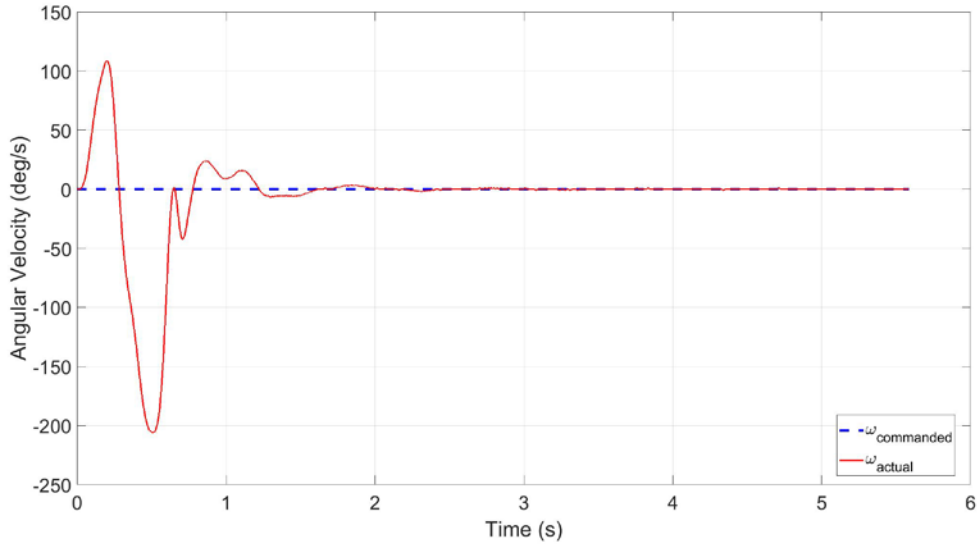

Figure 39. Baseline PD controller response: Elbow link angular velocity

Figure 40 is a plot of the shoulder and elbow currents during the maneuver.

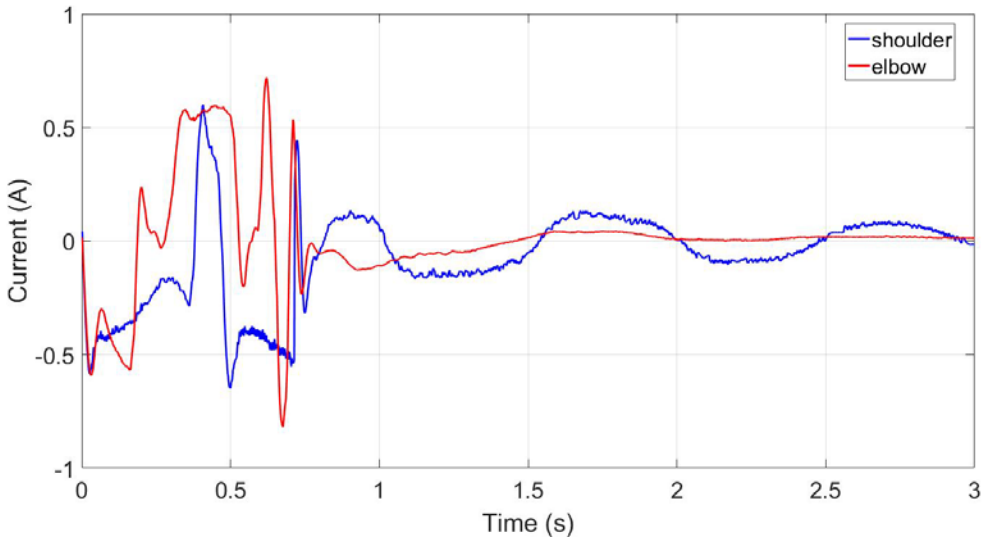

Figure 40. Baseline PD controller response: Shoulder and elbow currents

Table 8 summarizes the performance of the baseline PD controller. Just as in Chapter IV, the 2% settling time was based on the actual final value of each link angle, and not the desired final value.

Table 8. Baseline PD controller performance summary

	Shoulder	Elbow
Steady state value	28.91°	-28.86°
Steady state error	1.09°	1.14°
Peak-to-peak magnitude	3.21°	4.24°
2% settling time	2.16 s	1.338 s

3. Open-Loop Optimal Response

Since the goal of the tests is to determine whether the optimal control trajectory can be implemented, the next step was to implement an open loop controller where the optimal current trajectories alone were used as the command signals for the joint actuators. This effectively eliminated the feedback current and modified equation (1.30) to read:

$$i_{total} = i_{ff} \; . \tag{1.32}$$

Plots of the actual and commanded currents are shown in Figures 41 and 42.

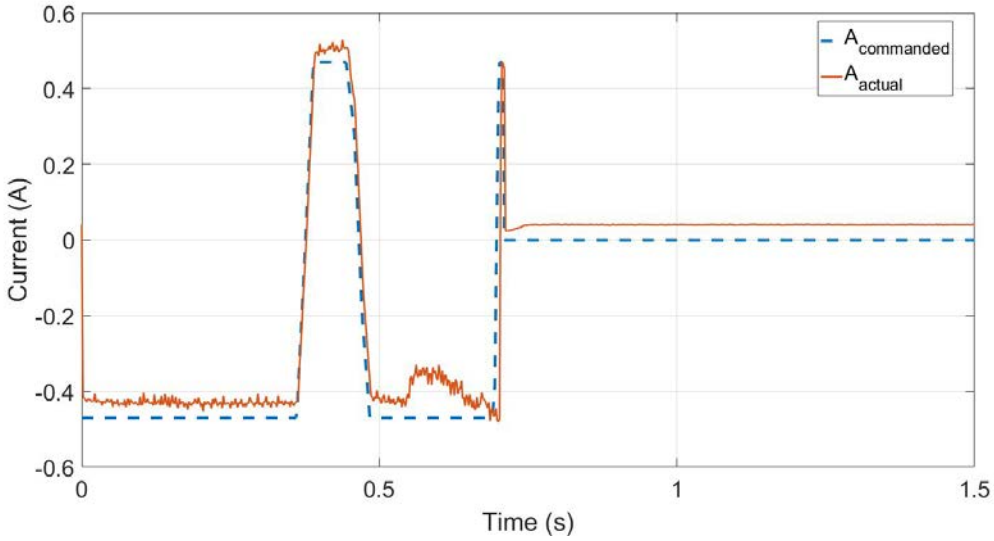

Figure 41. Response for open-loop optimal control: Shoulder actuator current

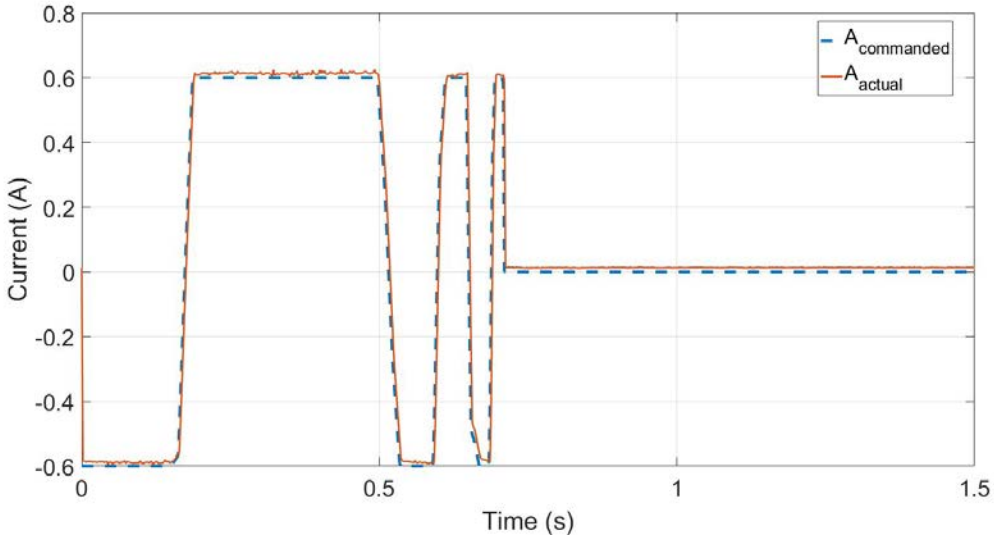

Figure 42. Response for open-loop optimal control: Elbow actuator current

Figure 43 and Figure 44 show the link angle response to the supplied current commands. The shoulder gets close to the desired value but the elbow has significant error.

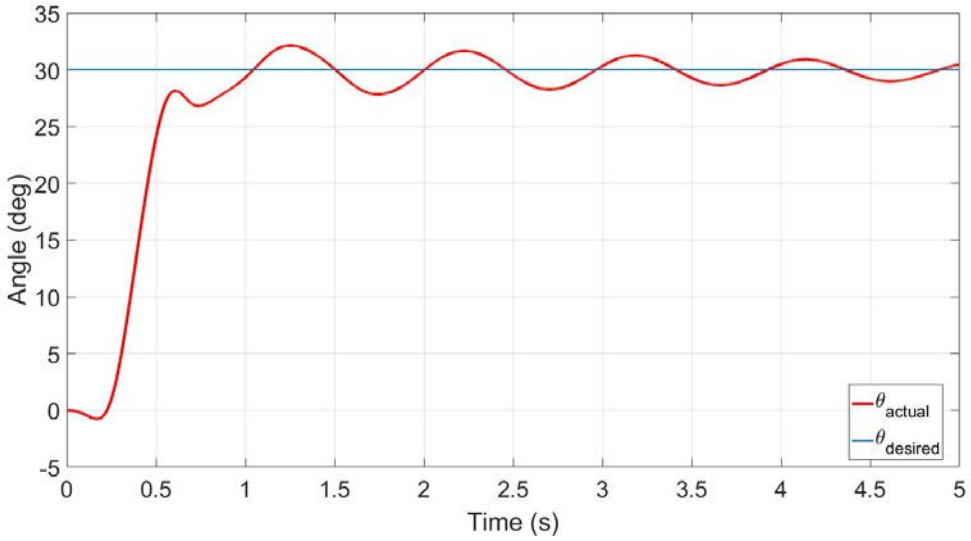

Figure 43. Response for open-loop optimal control: Shoulder link angular displacement

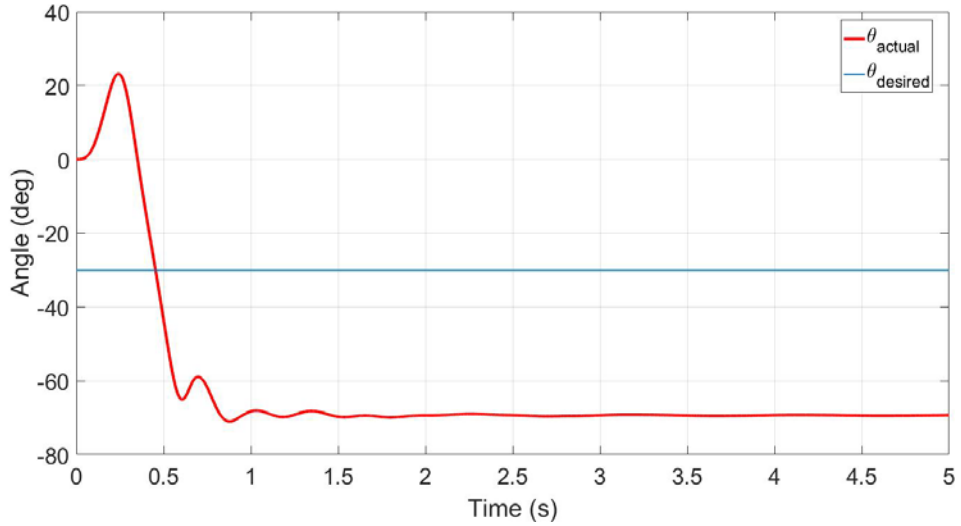

Figure 44. Response for open-loop optimal control: Elbow link angular displacement

Table 9 is a summary of the performance of the open loop optimal maneuver. The settling times are based off of the actual final values, not the desired final values.

Table 9. Open loop optimal maneuver performance summary

	Shoulder	Elbow
Steady state value	29.92°	-69.34°
Steady state error	0.08°	39.34°
Peak-to-peak magnitude	4.28°	2.98°
2% settling time	5.622 s	0.902 s

Open loop control is only expected to be feasible if the system model and parameters are known to a high degree of accuracy. The current model of the 2DOFSFJ, specifically the model parameters, is not accurate enough to provide satisfactory results. One way to improve performance, even without better system knowledge, is to implement feedback based solution.

4. Partial-State Feedback

The simplest feedback control relies only on feedback of the rotor shafts. Thus, the next step was to test a closed loop controller where the joint shaft angles and angular rates were used for feedback, along with current feed forward. The angular displacement plots are shown in Figure 45 and Figure 46. The shoulder reaches a steady state error of approximately 2°, and the elbow error is under 1°.

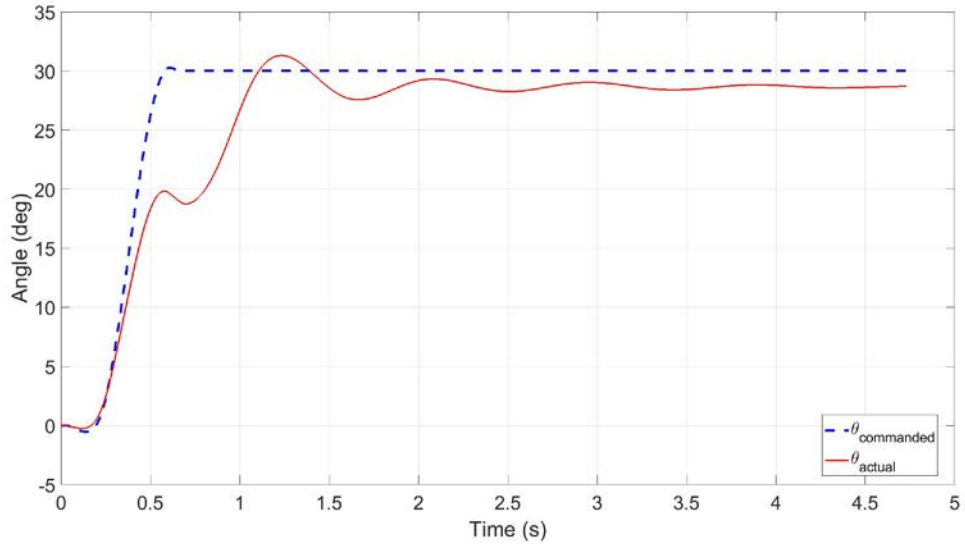

Figure 45. Response for partial-feedback optimal control: Shoulder link angular displacement

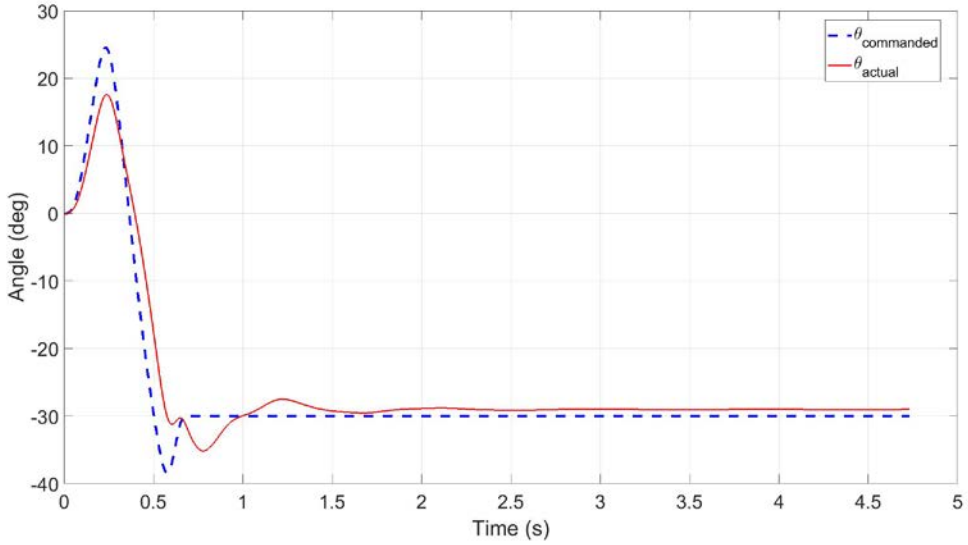

Figure 46. Response for partial-feedback optimal control: Elbow link angular displacement

Figure 47 and Figure 48 show the angular velocities of the shoulder and elbow links, respectively. The elbow reaches the steady state well before the shoulder does.

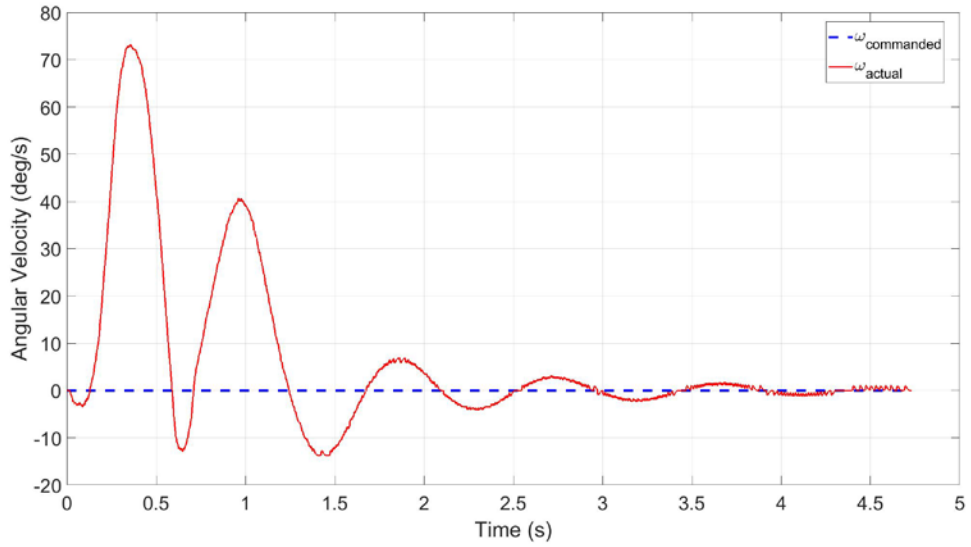

Figure 47. Response for partial-feedback optimal control: Shoulder link angular velocity

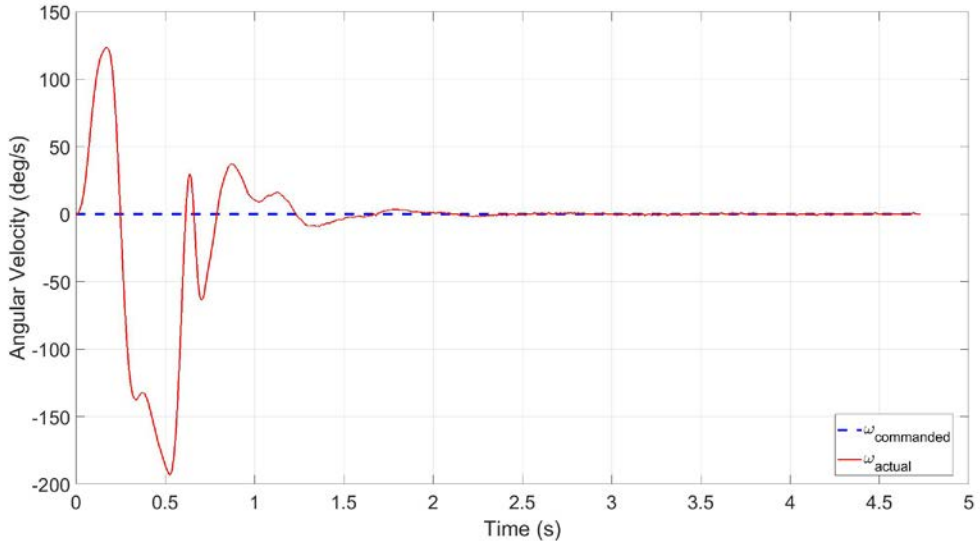

Figure 48. Response for partial-feedback optimal control: Elbow link angular velocity

Figure 49 is a plot of the shoulder and elbow currents during the maneuver.

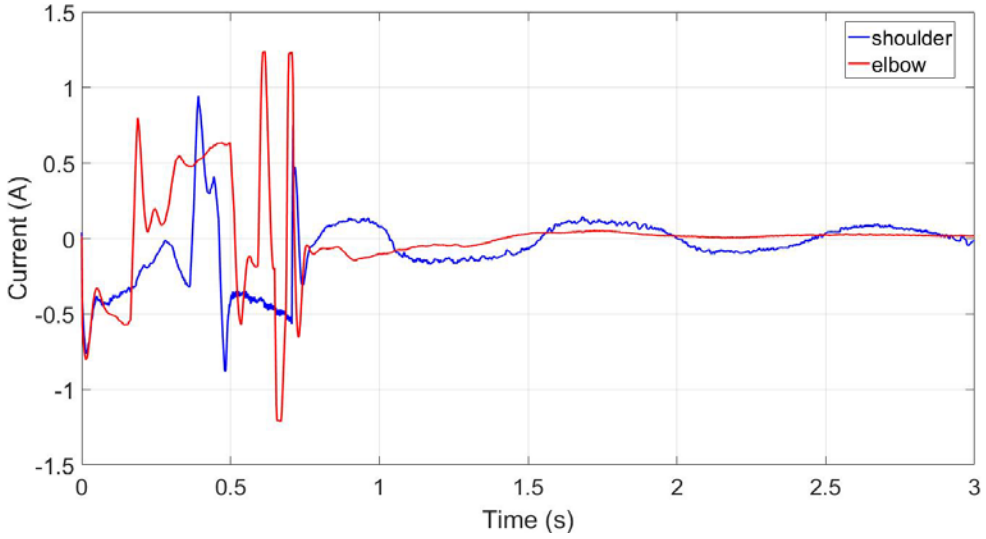

Figure 49. Response for partial-feedback optimal control: Shoulder and elbow currents

The performance of the optimal control maneuver implemented using partial state feedback is summarized in Table 10.

Table 10. Partial-state feedback optimal maneuver performance summary

	Shoulder	Elbow
Steady state value	28.7°	-29.05°
Steady state error	1.3°	0.95°
Peak-to-peak magnitude	3.74°	8.0°
2% settling time	2.136 s	1.362 s

5. Full-State Feedback

Next, a closed-loop controller where the trajectories for the shaft angle, shaft angular rate, link angle, and link angular rate were fed back for both the elbow and shoulder (i.e., full-state feedback), and the current was fed forward. This implementation used equation (1.32) without modification. The steady state error for the shoulder and elbow are similar to the other tests, but the trajectories that the links follow are nearly identical to the commanded optimal trajectories. Thus, it is possible to use the full-state feedback controller to correctly implement the optimal maneuver. The results of the experiment are shown in Figure 50 and Figure 51, where the commanded signals are blue dashes and the actual trajectories are in red. The discrepancy between the commanded and actual curves is a result of correcting for inaccurate knowledge of the system parameters via the feedback mechanism.

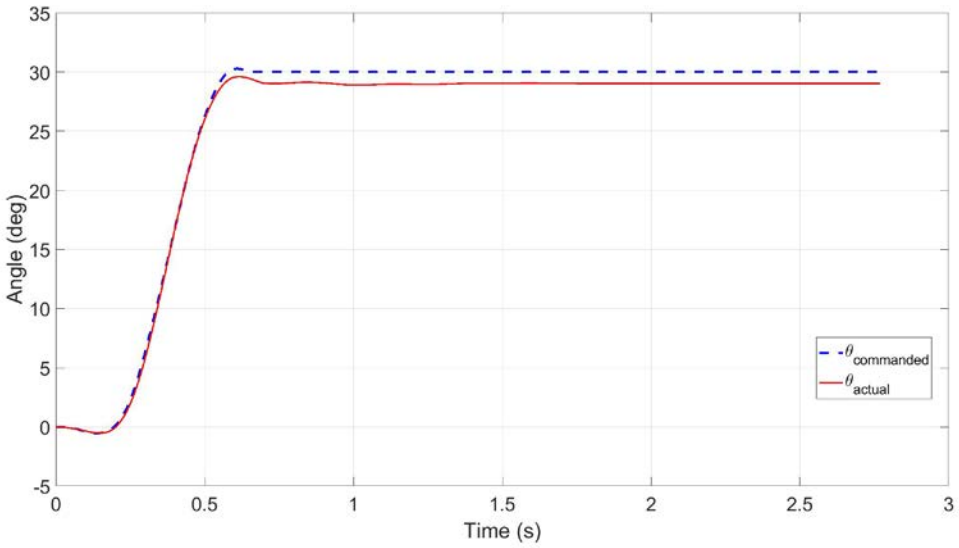

Figure 50. Response for full-state feedback optimal control: Shoulder link angular displacement

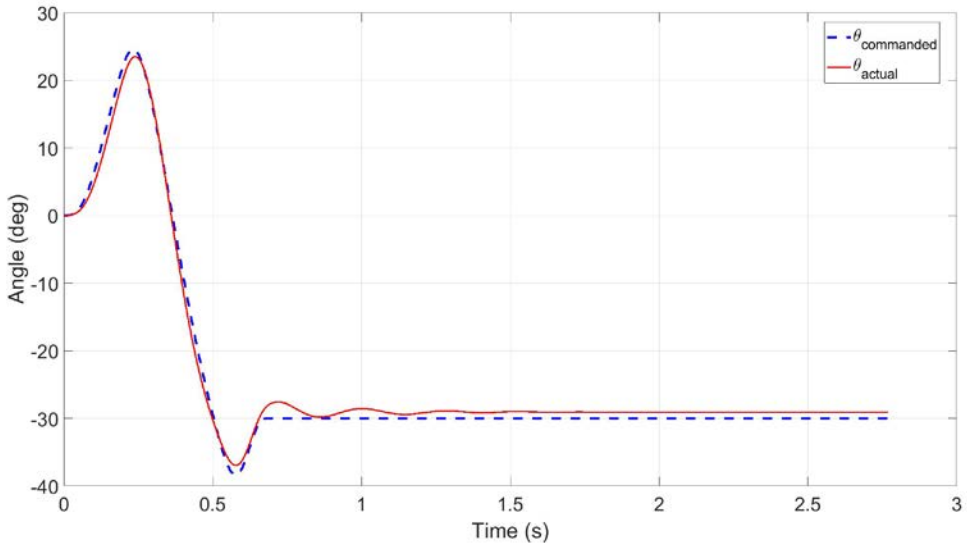

Figure 51. Response for full-state feedback optimal control: Elbow link angular displacement

The plots of the actual link angular velocities in Figure 52 and Figure 53 show that the experimental results match up almost identically with the commanded velocities.

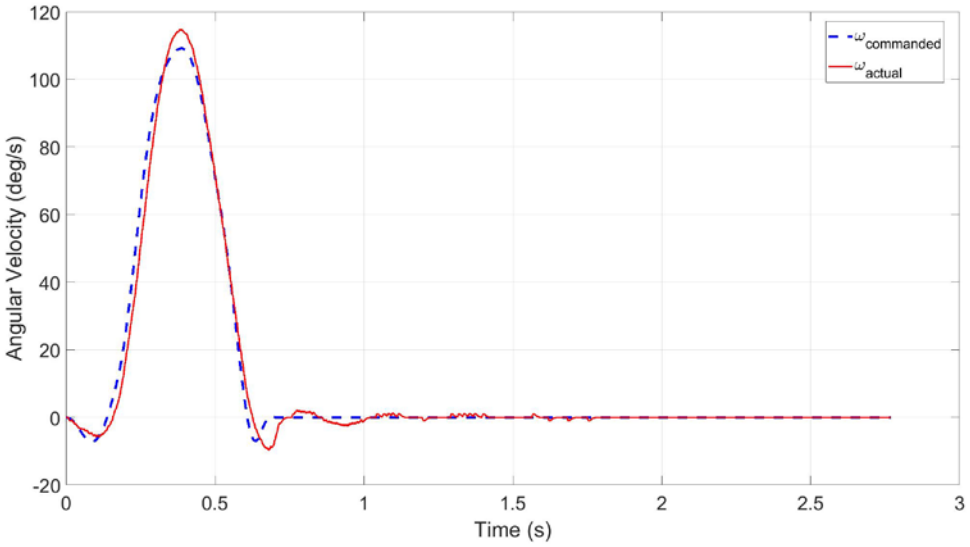

Figure 52. Response for full-state feedback optimal control: Shoulder link angular velocity

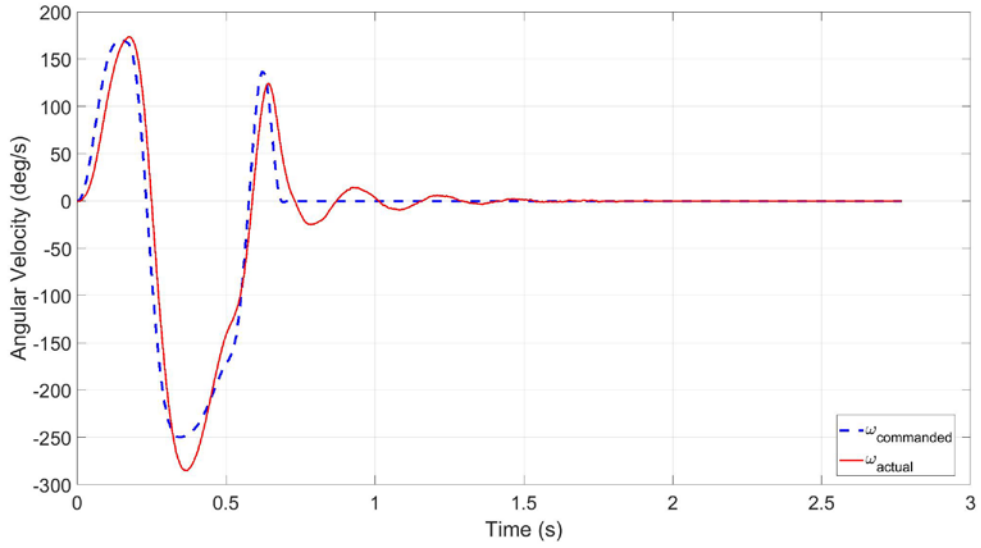

Figure 53. Response for full-state feedback optimal control: Elbow link angular velocity

Figure 54 is a plot of the shoulder and elbow currents during the maneuver.

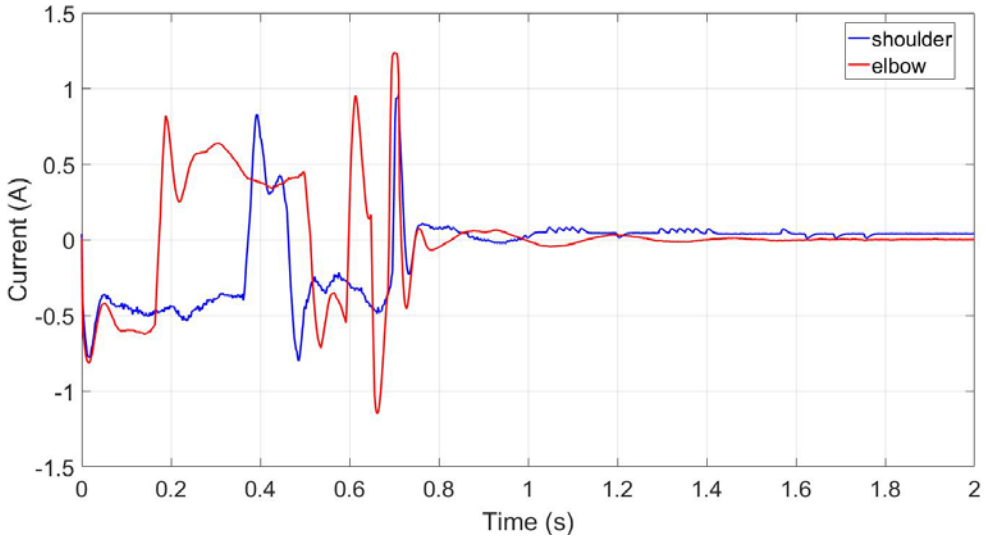

Figure 54. Response for full-state feedback optimal control: Shoulder and elbow currents

The performance metrics of the optimal control maneuver using full-state feedback is summarized in Table 11.

Table 11. Full-state feedback optimal maneuver performance summary

	Shoulder	Elbow
Steady state value	29.02°	-29.06°
Steady state error	0.98°	0.94°
Peak-to-peak magnitude	0.59°	2.25°
2% settling time	0.624 s	0.892 s

D. COMPARISON OF OPTIMAL AND BASELINE MANEUVERS

Since the optimal control maneuver with full-state feedback appeared to perform the best in the trials, it was used in a side-by-side analysis against the baseline PD controller. Ten separate experiments were run for each the optimal and PD controllers to test repeatability. The results are very repeatable, and it is only by enlarging the scale that the separate curves begin to appear, as in Figure 55.

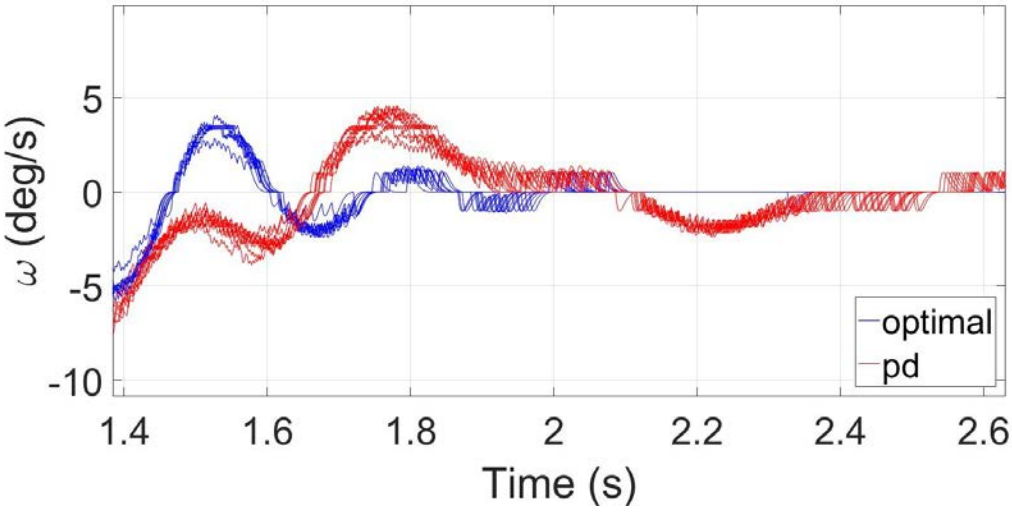

Figure 55. Enlarged view of the elbow link angular velocities from 10 runs

To compare the baseline and optimal maneuver, Figures 56 through 63 show the optimal control commanded trajectory in magenta and the commanded PD trajectory in green, along with the actual optimal and PD results, in blue and red respectively.

1. Actual versus Commanded Trajectories

The side-by-side comparison of the PD and optimal controllers, along with the comparison between the actual and commanded trajectories, is quite revealing. The actual optimal trajectories are very close to the commanded trajectories, so the response is quite predictable. On the other hand, the PD trajectories lag the command. This makes sense because the PD control system was set up to track only the desired shaft and link angle profiles. Matters would be improved by using additional inputs to the PD system, but at the best the baseline system would produce the green trace, which is significantly slower than the optimal response, in red.

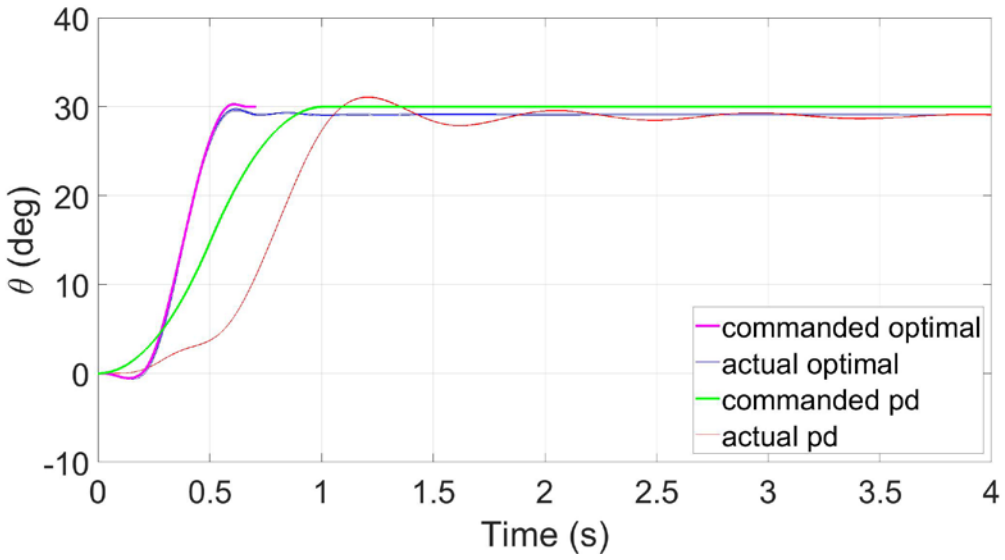

Figure 56. Comparison of baseline and optimal maneuvers: Shoulder link angular displacement

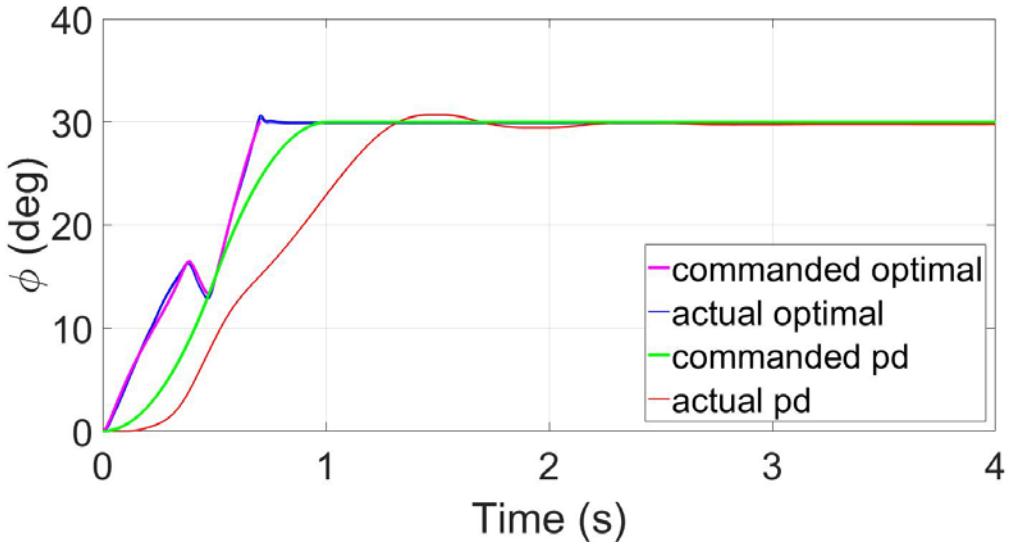

Figure 57. Comparison of baseline and optimal maneuvers: Shoulder shaft angular displacement

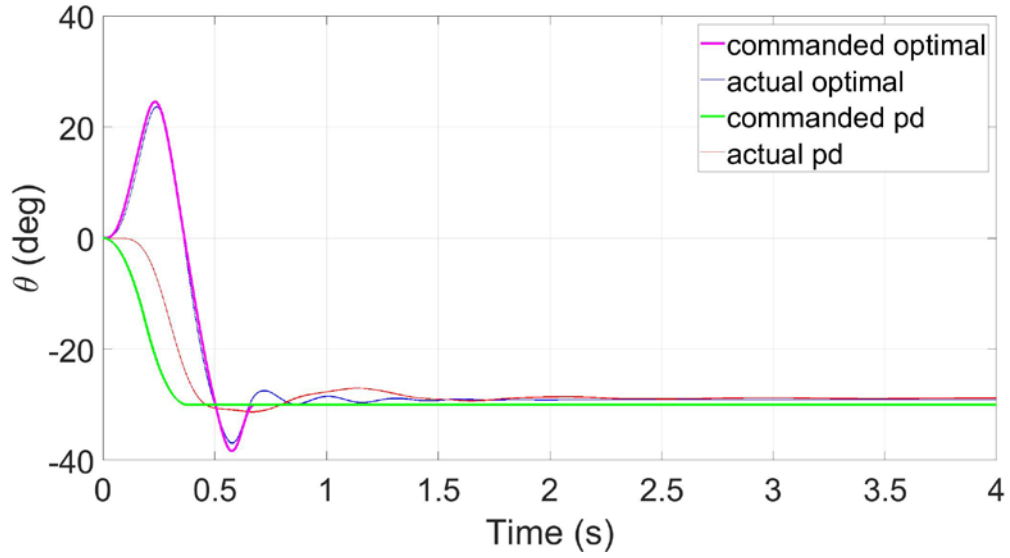

Figure 58. Comparison of baseline and optimal maneuvers: Elbow link angular displacement

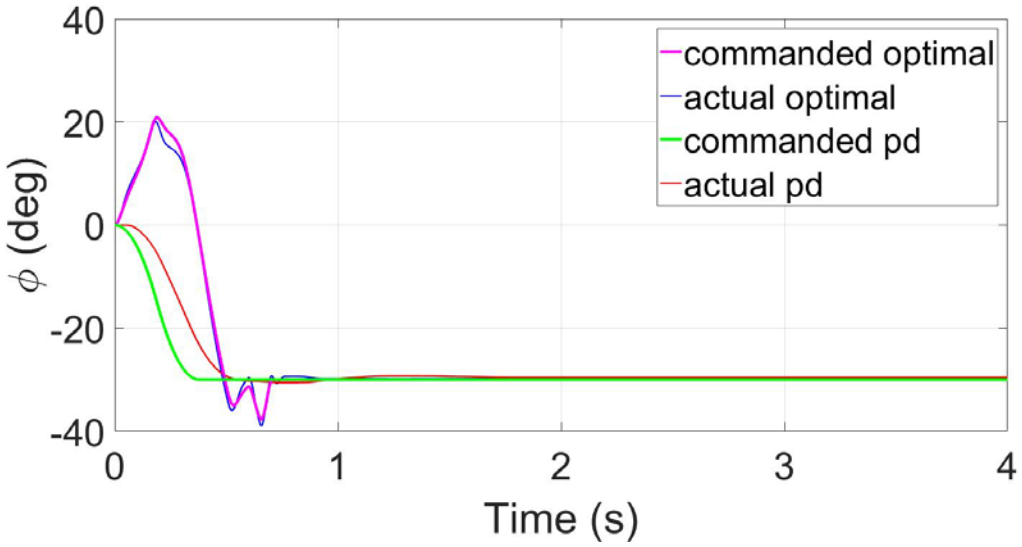

Figure 59. Comparison of baseline and optimal maneuvers: Elbow shaft angular displacement

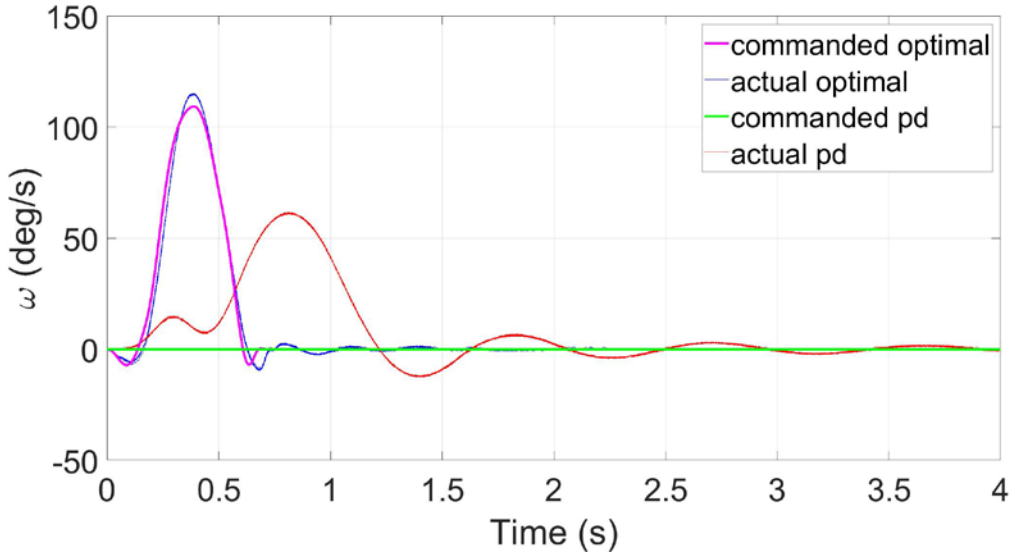

Figure 60. Comparison of baseline and optimal maneuvers: Shoulder link angular velocity

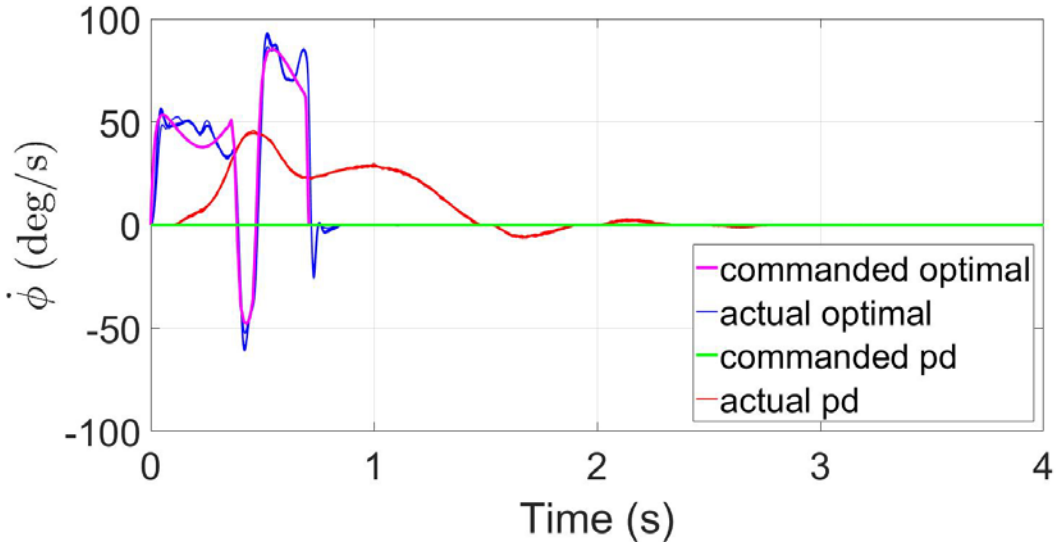

Figure 61. Comparison of baseline and optimal maneuvers: Shoulder shaft angular velocity

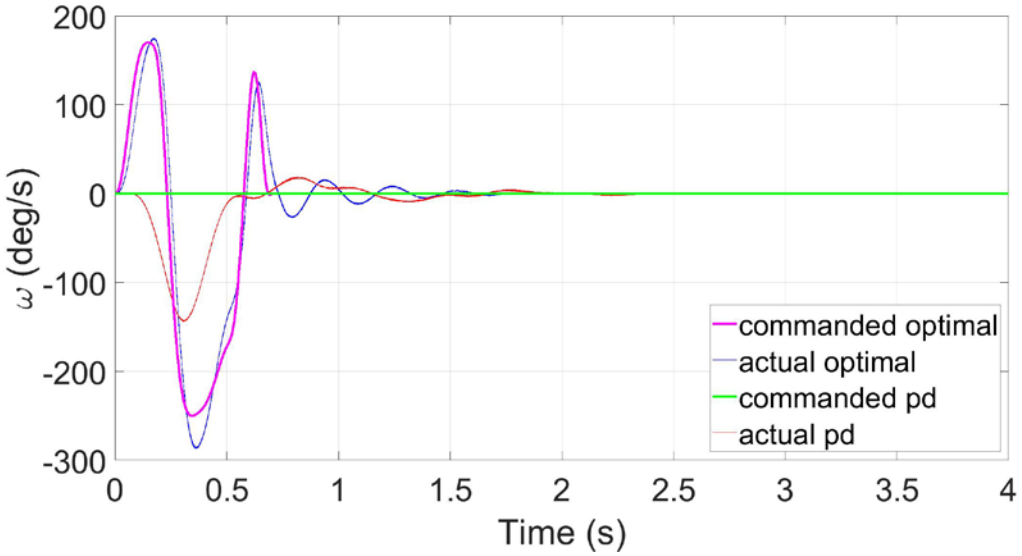

Figure 62. Comparison of baseline and optimal maneuvers: Elbow link angular velocity

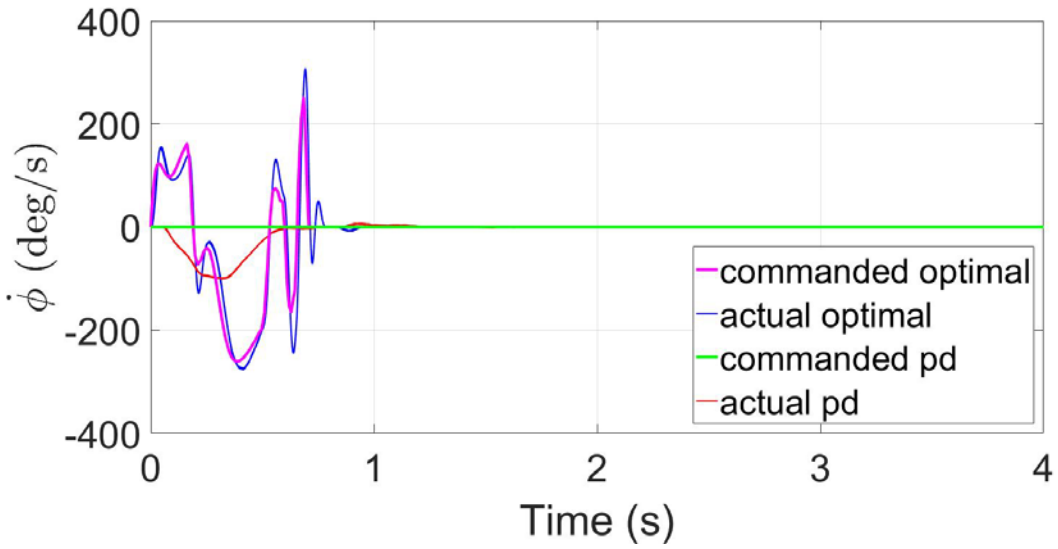

Figure 63. Comparison of baseline and optimal maneuvers: Elbow shaft angular velocity

2. Average Curves

While the optimal controller appears visually to perform better than the PD controller, it is difficult to quantify the overall difference in performance with these plots. The average of the ten optimal and ten PD experiments can be taken, and the result plotted. Then the average will be evaluated for when the angles reach within ±2% of the final angle. These results can then be compiled for ease of comparison. Figures 64 through 67 show the average curves, along with reference lines at ±2% from the final values. These reference lines are used to determine settling times.

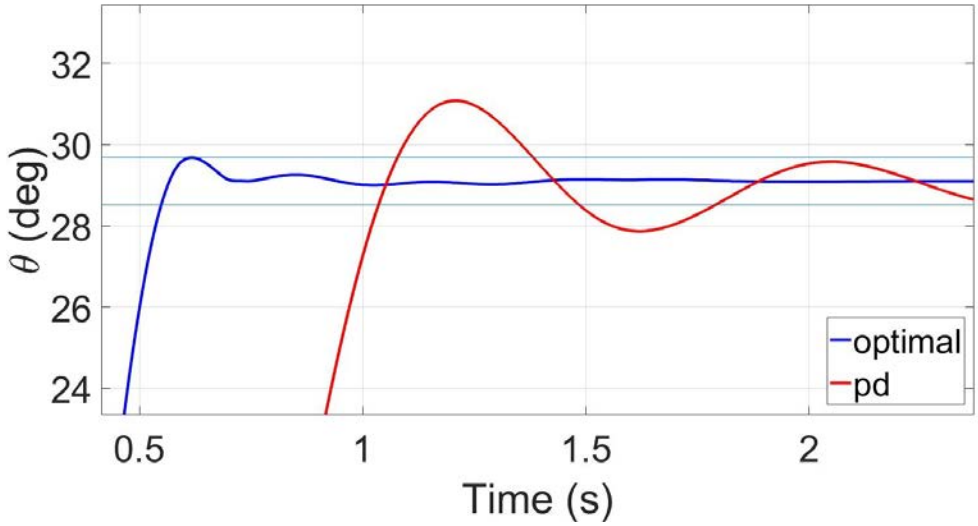

Figure 64. Schematic showing the shoulder link angular displacement settling time

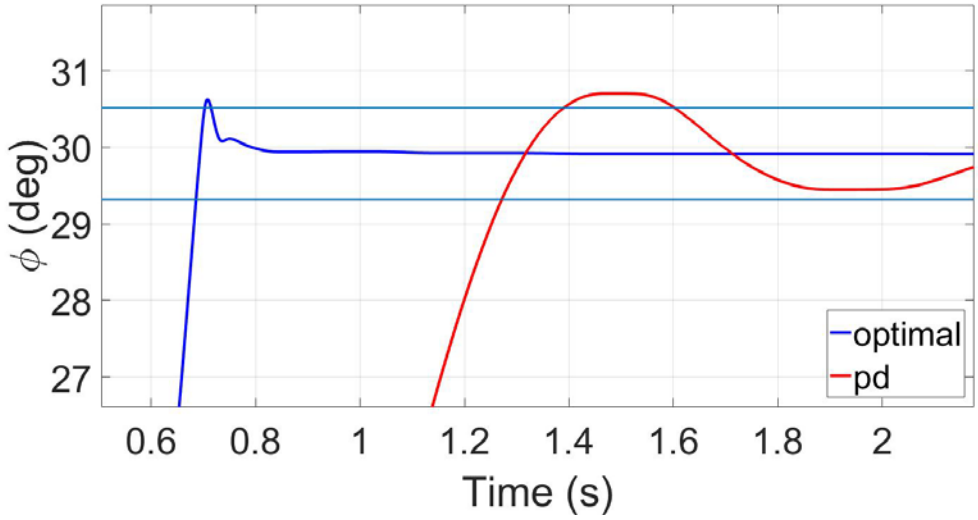

Figure 65. Schematic showing the shoulder shaft angular displacement settling time

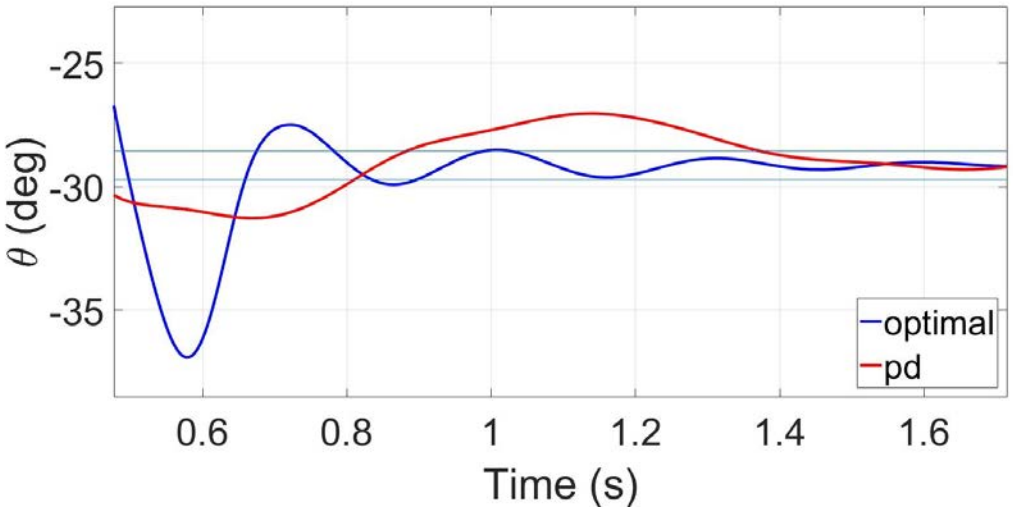

Figure 66. Schematic showing the elbow link angular displacement settling time

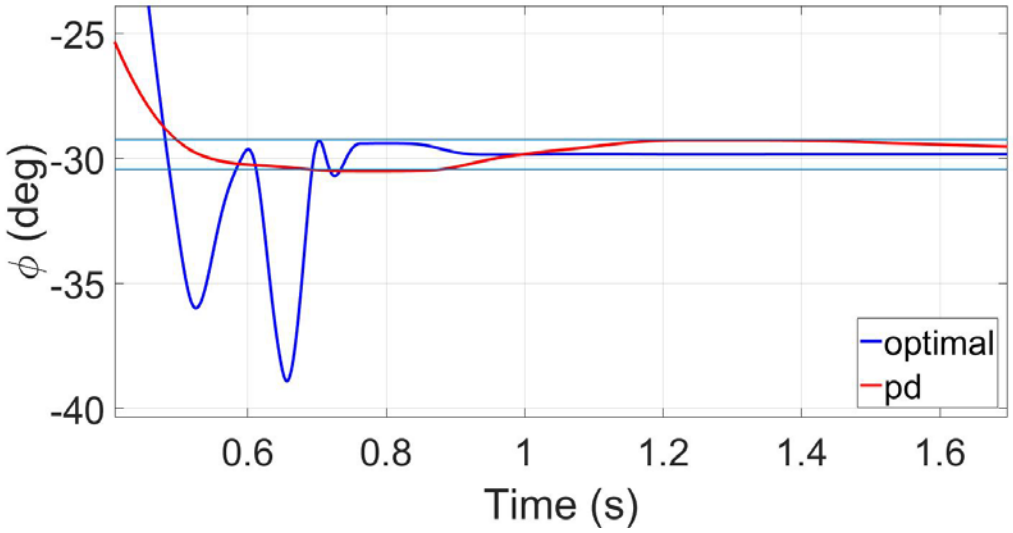

Figure 67. Schematic showing the elbow shaft angular displacement settling time

E. INTERPRETING THE RESULTS

A summary of the results is shown in Table 12, Table 13, and Table 14. These results clearly show that the optimal controller using full-state feedback is superior to the PD controller.

Table 12. Experimental steady state values

	Steady state value PD	Steady state value optimal	Steady state error PD	Steady state error optimal
Shoulder shaft φ	29.79°	29.92°	0.21°	0.08°
Shoulder link θ	28.99°	29.10°	1.01°	0.90°
Elbow shaft φ	-29.55°	-29.84°	0.45°	0.16°
Elbow link θ	-28.86°	-29.14°	1.14°	0.86°

Table 13. Experimental 2% settling times

	PD settling time (s)	Optimal settling time (s)	Percent difference
Shoulder shaft φ	1.63	0.72	56%
Shoulder link θ	2.07	0.55	73%
Elbow shaft φ	0.93	0.74	20%
Elbow link θ	1.34	1.03	23%
Total response	2.07	1.03	50%

Table 14. Experimental peak-to-peak magnitude

	PD	Optimal	Percent difference
Shoulder shaft φ	1.25°	0.55°	56%
Shoulder link θ	3.21°	0.58°	82%
Elbow shaft φ	1.29°	1.42°	9%
Elbow link θ	4.24°	2.43°	43%
Total response	4.24°	2.43°	43%

Table 12 shows that the optimal maneuver using full-state feedback produces less error than the PD controller in all four cases. Table 13 shows that the optimal maneuver was faster by 50%. Table 14 is an analysis of the peak-to-peak magnitude of the vibration. The optimal maneuver had smaller vibrations in three out of the four cases. Even with a significantly faster maneuver, the steady state errors produced with the optimal maneuver are all much smaller than the errors produced with the PD controller. This shows that the optimal controller can produce a faster maneuver with less error and less residual vibration.

The optimal maneuver was calculated to take 0.7084 s, and as implemented took 1.03 s, using the longest settling time for angular displacement. This is an increase of 45%. The baseline maneuver theoretically should take 1.002 seconds, but as implemented took at 2.07 seconds, an increase of nearly 107%.

In every measure, whether time to complete the maneuver, steady state error, remaining vibrations, or predicted vs actual time, the optimal maneuver outperformed the standard baseline solution.

F. CHAPTER SUMMARY

This chapter sought to experimentally verify that an optimal control maneuver could be successfully implemented on the 2DOFSFJ. In order to do this, the mathematical model was modified from the one designed in Chapter II. This model was analyzed and run through DIDO to generate the optimal control trajectories that would be needed for experimental validation. In order to have a baseline comparison, a standard PD controller was used to move the 2DOFSFJ links to the desired positions. Following that experiment, the optimal control maneuver current trajectories were implemented on the 2DOFSFJ in an open loop. A closed loop configuration was then run, with feedback on the elbow and shoulder shafts, and current feed forward. A successful experiment with full-state feedback, and current feed forward, was completed, and analysis was done to evaluate which configuration was the most successful. The optimal control solution using the full-state feedback controller completed the maneuver in the fastest time, with the least error and with the least residual vibration.

THIS PAGE INTENTIONALLY LEFT BLANK

VI. CONCLUSIONS AND FUTURE WORK

While this thesis has made significant contributions to the overall research goal of optimal cooperative maneuvering of flexible multi-body spacecraft, there is still much work to be done.

A. SUMMARY OF WORK

This thesis started on the foundation provided by previous students [10], [12]. The experimental testbed was upgraded, with several important additions designed and constructed at NPS, and many components improved. The reaction wheel array will enable the ultimate research goal of cooperative maneuvers, while the wireless power and command and control systems will provide for more representative experiments. The 2DOFSFJ was a major addition to the MBSS. It is an ideal system for testing the optimal control maneuvers. An example minimum time maneuver was tested in several different configurations. First, a standard PD controller was used to establish a baseline. Then the optimal control current commands were used in an open loop. A closed loop controller was demonstrated, using feedback from the joint actuator shafts. Finally, a closed loop controller was implemented that used feedback from the shafts and the link encoders, as well as current feed forward, to arrive at a very effective solution. The time-optimal maneuver could reduce the overall time by 50% with less error and residual vibration than a standard control law.

B. FUTURE WORK

1. Fully Integrate Hardware on MBSS

At the completion of this thesis research the MBSS is a collection of highly capable subsystems mounted on a common frame, but lacking the software integration necessary to perform the desired cooperative maneuver testing. Specifically, the passive flexible appendage needs to be instrumented with sensors to measure its angular displacement and angular velocity. Its physical properties, such as mass and moment of inertia, should also be quantified in the laboratory setting.

The reaction wheel array needs to be brought to life. The individual Maxon DC motors function, as verified using an analog controller. However, they have not been tested with the EPOS digital motor controllers. The reaction wheels must be tested to see if they provide enough torque and momentum for the MBSS. Pending a successful test, the reaction wheel mount can then be redesigned for a standard pyramid configuration.

The National Instruments cRIO has not been integrated with the other electronics. The National Instruments LabVIEW software will be used to develop the correct command and data acquisition system. While LabVIEW is advertised as being compatible with the other hardware on the MBSS, the integration will be no small feat.

The power supply needs to be fully vetted. While the reaction wheels and their associated motor controllers, as well as the cRIO, can all function on battery power, the 2DOFSFJ has not been tested with the battery. The 2DOFSFJ has much more stringent power requirements, and will require that additional power amplifiers are added to the MBSS before it can be truly wireless.

2. Improve the Mathematical Model

The non-linear dynamical mathematical model of the 2DOFSFJ is reasonable, but it can be improved. The physical properties of the 2DOFSFJ should be verified experimentally, much as the springs were. Specifically, the link and shaft moments of inertia and the damping ratios should be tested. This will allow for a better model fidelity that will be necessary when performing cooperative maneuvers. Conversely, the optimal control model could be altered to allow it to incorporate uncertainty. This would be very useful when integrating the 2DOFSFJ with the rest of the MBSS. Since the overall system will rapidly outpace the ability to accurately test the mass properties of each element, much less the MBSS as a whole, the mathematical model must be able to accommodate the changing characteristics that will results from adding sensors of altering cable routing. A multi-body dynamical model of the full MBSS should also be developed.

3. Incorporate Reaction Wheels into Maneuver

The most important endeavor that needs to take place is incorporating the reaction wheels into a cooperative maneuver with the 2DOFSFJ. This effort is essential to the overall research goals, but can only take place once the other two objectives are met. This will be a demanding task, requiring a highly accurate mathematical model of the system and a fully functioning testbed infrastructure. Further, it will be important to derive the correct metrics on which to evaluate the maneuver. While minimum time maneuvers are valuable, it may be more important to deliver a minimum energy maneuver or to consider other cost functionals.

THIS PAGE INTENTIONALLY LEFT BLANK

LIST OF REFERENCES

[1] E. T. Stoneking, "Newton-Euler dynamic equations of motion for a multi-body spacecraft," in *AIAA Guidance, Navigation and Control Conference*, 2007. [Online]. doi: 10.2514/6.2007-6441.

[2] L. Shunli, Y. Xu, and D. Yang, "Active disturbance rejection control for high pointing accuracy and rotation speed," *Automatica*, vol. 45, no. 8, pp. 1854–1860, Aug. 2009.

[3] P. Huang, Y. Xu, and B. Liang, "Balance control of multi-arm free-floating space robots during capture operation," in *IEEE International Conference on Robotics and Biomimetics*, 2005, pp. 398–403.

[4] B. Ekstrand, "Equations of motion for a two-axis gimbal system," *IEEE Transactions on Aerospace and Electronics Systems*, vol. 37, no. 3, pp. 1084–1091, Jul. 2001.

[5] B. Bishop, R. Gargano, A. Sears, and M. Karpenko, "Rapid maneuvering of multi-body dynamic systems with optimal motion compensation," *Acta Astronautica*, vol. 117, pp. 209–221, Aug. 10, 2015.

[6] S. Leyendecker, S. Ober-Blobaum, J. E. Marsden, and M. Ortiz, 2010, "Discrete mechanics and optimal control for constrained systems," *Optimal Control Applications and Methods*, vol. 31, no. 6, pp. 505–328, Nov. 2010.

[7] C. L. Bottasso and A. Croce, "Optimal control of multibody systems using an energy preserving direct transcription method," *Multibody System Dynamics*, vol. 12, no. 1, pp. 17–45, Aug. 2004.

[8] G. N. Jazar and A. Naghshineh-Pour, "Floating time algorithm for time optimal control of multi-body dynamic systems," *Proceedings of the Institution of Mechanical Engineers, Part K: Journal of Multi-body Dynamics*, vol. 219, no. 3, pp. 225–236, Sep. 1, 2005.

[9] M. Gerdts, "Optimal control and real-time optimization of mechanical multi-body systems," *Journal of Applied Mathematics and Mechanics*, vol. 83, no. 10, pp. 705–719, Sep. 10, 2003.

[10] M. J. Griggs, "Experimental test rig for optimal control of flexible space robotic arms," M.S. thesis, Dept. of Mech. and Aero. Eng., NPS, Monterey, CA, USA, 2016. [Online]. Available: https://calhoun.nps.edu/handle/10945/51706

[11] M. W. Spong, "Modeling and control of elastic joints," *Journal of Dynamic Systems, Measurement, and Control*, vol. 109, no. 4, pp. 310–319, Dec. 1, 1987.

[12] S. W. Wojdakowski, “Rapid slewing of flexible space structures,” M.S. thesis, Dept. of Mech. and Aero. Eng., NPS, Monterey, CA, USA, 2015. [Online]. Available: https://calhoun.nps.edu/handle/10945/47347

[13] I. M. Ross, *A Primer on Pontryagin’s Principle in Optimal Control*. San Francisco, CA, USA: Collegiate Publishers, 2009.

[14] “Dynamixel Pro,” Robotis. Accessed October 30, 2017. [Online]. Available: http://www.robotis.us/dynamixel-pro/

[15] “Maxon EC flat motors,” Maxon Motors. Accessed October 30, 2017. [Online]. Available: https://www.maxonmotorusa.com/maxon/view/content/index

[16] B. Wie, *Space Vehicle Dynamics and Control*, 2nd ed. Reston, VA, USA: The American Institute of Aeronautics and Astronautics, 2008.

[17] “CompactRIO controller,” National Instruments. Accessed October 30, 2017. [Online]. Available: http://www.ni.com/en-us/shop/select/compactrio-controller

[18] “2 DOF serial flexible joint,” Quanser. Accessed October 30, 2017. [Online]. Available: https://www.quanser.com/products/2-dof-serial-flexible-joint/

INITIAL DISTRIBUTION LIST

1. Defense Technical Information Center
   Ft. Belvoir, Virginia

2. Dudley Knox Library
   Naval Postgraduate School
   Monterey, California